Cauchy horizon stability and instability of regular black holes

Alfio Bonanno*

INAF, Osservatorio Astrofisico di Catania, via Santa Sofia 78, I-95123 Catania, Italy and INFN, Sezione di Catania, via Santa Sofia 64, I-95123 Catania, Italy

Antonio Panassiti†

INAF, Osservatorio Astrofisico di Catania, via Santa Sofia 78, I-95123 Catania, Italy; INFN, Sezione di Catania, via Santa Sofia 64, I-95123 Catania, Italy; Dipartimento di Fisica e Astronomia "Ettore Majorana," Università di Catania, via Santa Sofia 64, 95123, Catania, Italy; and High Energy Physics Department, Institute of Mathematics, Astrophysics, and Particle Physics, Radboud University, Heyendalseweg 135, 6525 AJ Nijmegen, The Netherlands

Frank Saueressig‡

High Energy Physics Department, Institute of Mathematics, Astrophysics, and Particle Physics, Radboud University, Heyendalseweg 135, 6525 AJ Nijmegen, The Netherlands

(Received 18 July 2025; accepted 20 July 2026; published 8 September 2026)

A common feature of regular black-hole spacetimes is the presence of an inner Cauchy horizon. The analogy to the Reissner-Nordström solution then suggests that these geometries suffer from a mass-inflation effect, rendering the Cauchy horizon unstable. Recently, it was shown that this analogy fails for certain classes of regular black holes, including the Hayward solution, where the late-time behavior of the mass function no longer grows exponentially but follows a power law. In this work, we extend these results in a twofold way. First, we determine the basin of attraction for the power-law attractor, showing that the tamed growth of the mass function is generic. Second, we extend the systematic analysis to the Bardeen and Dymnikova geometries, the Ghosh-Culetu black hole, and a spacetime arising from a nonsingular collapse model newly proposed in the context of asymptotically safe quantum gravity. Remarkably, in the latter solution, the Misner-Sharp mass at the Cauchy horizon remains of the same order of magnitude of the mass of the black hole, since its growth is just logarithmic.

DOI: 10.1103/34w6-s2yl

I. INTRODUCTION

Black holes are among the most fascinating objects in theoretical physics [1,2]. Arguably, a thorough understanding of these objects may the key toward understanding the working of gravity in the strong gravity regime or at the level of a quantum theory. Within classical general relativity black holes are rather simple objects. Essentially, the corresponding static solutions consist of a spacetime singularity which is hidden inside an (outer) event horizon. Once charge is added, the Schwarzschild solution generalizes to the Reissner-Nordström (RN) geometry. Besides the event horizon, this geometry also comes with an (inner) Cauchy horizon (CH). As first suggested by Penrose [3] and subsequently verified in [4–6], the CH appearing in the RN solution is unstable and suffers from a mass-inflation effect. In short, the cross-flow of ingoing and outgoing matter leads to an eternal, exponential growth of the mass function at the CH.

This instability for the RN black hole, and other geometries containing timelike singularities, also persists at the level of quantum field theory in curved spacetime. Studying the growths of the expectation value of the stress energy tensor of a scalar field at the CH, it was shown that quantum effects do not cure the instability [7–17]. This conclusion also persists when the RN black hole is embedded into de Sitter space [18,19]. So quantum effects do not tame the mass-inflation instability in these cases.

The breakdown of the laws of physics at a spacetime singularity motivates the construction of regular black-hole geometries which resolve this singularity in one way or another. Starting from the works by Bardeen [20,21], there is now a rich literature on this subject [22–26], including the proposals by Dymnikova [27–29], Bonanno-Reuter [30,31], Hayward [32], Simpson-Visser [33], the Ghosh-Culetu class [34–36], and lately also the regular geometries obtained

*Contact author: alfio.bonanno@inaf.it
†Contact author: antonio.panassiti@phd.unict.it
‡Contact author: f.saueressig@science.ru.nl

from a model of gravitational collapse within the gravitational asymptotic safety program [37]. Moreover, there is currently a significant effort in obtaining such solutions from dynamical principles, e.g., by resorting to nonlinear electrodynamics [38–41] or studying infinite towers of curvature monomials [42]. A feature frequently encountered in these regular geometries is that they also possess a CH, making the geometry similar to the (RN) solution.[1] On this basis, it was believed for a long time that also regular black holes exhibiting a CH would suffer from the mass-inflation instability, rendering the CH singular [45–47].

Returning to the classical analysis, the study of the Ori model [6] (also see Refs. [48,49] for reviews) for regular black-hole geometries revealed a remarkable feature: in some cases, including the Hayward geometry and the Bonanno-Reuter black holes, the exponential growth of the mass function is replaced by a power-law scaling [50,51]. Moreover, the character of the singularity building up at the CH may change from a strong to a weak singularity [50,51] according to the definitions given in [6,52–56]. Ultimately, these drastic deviations from the RN analysis can be traced back to the fact that the equation determining the dynamics of the mass function is no longer linear but quadratic in the mass. This leads to new late-time behaviors that are absent in the RN analysis.

The present work expands on this picture in two ways. Building on the Ori model [6], we present a complete phase space analysis for the regular black holes of Bardeen [20], Hayward [32], Dymnikova [27], Ghosh-Culetu [34], and asymptotically safe (AS) collapse [37]. In all cases, we identify the quasifixed points governing the late-time dynamics of the models. For the Hayward geometry, this reveals that the conversion of the mass-inflation effect to a transient phenomenon is generic. The power-law attractor controlling the late-time dynamics is reached from generic initial conditions. The study of the Dymnikova, Ghosh-Culetu, and AS-collapse model extends the systematic study to regular black holes whose mass functions are not a rational functional of the radial coordinate. For the Dymnikova and Ghosh-Culetu case, it is shown that the phase space has a rich structure in which eternal mass inflation is rather generic. In contrast, the growth of the mass function obtained from the AS-collapse model is weaker than power law and only growths logarithmically. Moreover, no appreciable transient mass-inflation episode occurs before the attractor is reached. The strength of the singularity building up in this case is even weaker than the one found for the Hayward case.

The rest of this paper is organized as follows. Section II introduces the geometries investigated here and briefly reviews the classical mass-inflation instability in RN. Section III summarizes the Ori model and its technical and physical assumptions. Section IV develops the general phase-space structure in terms of quasifixed points. The dynamics for the selected regular black holes are presented in Sec. V. We conclude in Sec. VI with a discussion and an outlook. Our curvature conventions are collected in Appendix A, figures for the CH dynamics of the Ghosh-Culetu class are integrated in Appendix B, and technical details for the analytic treatment of the AS-collapse model are given in Appendix C. Throughout we set Newton's constant to $G_{\mathrm{N}} = 1$, so that all dimensionful quantities are measured in Planck units.

II. CAUCHY HORIZON INSTABILITY

We are interested in spherically symmetric black-hole geometries. In this case, one can always find coordinates such that the line element takes the form

$$ds^2 = g_{ab}dx^a dx^b + r^2 d\Omega^2, \qquad a, b = 0, 1. \tag{1}$$

Here $d\Omega^2 = d\theta^2 + \sin^2\theta d\phi^2$ and $r = r(x^a)$ is the areal radius of the 2-sphere at the point x^a. We then introduce the Misner-Sharp mass $M(x^a)$ via

$$f(x^a) \equiv g^{ab}\partial_a r \partial_b r = 1 - \frac{2M(x^a)}{r}. \tag{2}$$

The function $M(x^a)$ measures the quasilocal energy inside the sphere of radius r and provides a convenient, coordinate-invariant characterization of spherically symmetric spacetimes. Static geometries are then completely fixed by the radial profile $M(r)$. In particular, the Schwarzschild metric has $M(r) = m$, where m is the ADM mass.

The examples studied in this work are specified by[2]

$$\text{RN:}\ M(r) = m - \frac{e^2}{2r}, \tag{3a}$$

$$\text{Bardeen:}\ M(r) = \frac{mr^3}{(r^2 + a^2)^{3/2}}, \tag{3b}$$

$$\text{Hayward:}\ M(r) = \frac{mr^3}{r^3 + 2ml^2}, \tag{3c}$$

$$\text{Dymnikova:}\ M(r) = m\left[1 - \exp\left(-\frac{r^3}{\gamma^2 m}\right)\right], \tag{3d}$$

$$\text{Ghosh-Culetu:}\ M(r) = m\exp\left(-\frac{\alpha^2}{2mr}\right), \tag{3e}$$

[1] Lately, this idea has spurred the development of regular black-hole geometries where the CH is absent [43,44].

[2] In (3f), with respect to [37], we implemented an analytic continuation of $M(r)$ so that the Misner-Sharp mass remains real for all values of m.

$$\text{AS-collapse}: \ M(r) = \frac{r^3}{12\xi}\log\left(1+\frac{6\xi m}{r^3}\right)^2. \quad (3f)$$

Here e denotes the electric charge in the RN solution. The remaining parameters $\{a, l, \gamma, \alpha, \xi\}$ characterize deviations from Schwarzschild/RN and set the short-distance scale at which the geometry is modified. The geometries (3b)–(3d) are standard examples of *regular* black holes with a nonsingular center, commonly interpreted as effective descriptions of new physics in the strong-curvature regime.

A natural organizing principle is the nature of the "core" [57]. The regular geometries (3b)–(3d) share the small-r behavior $M(r) = cr^3 + O(r^5)$ with $c > 0$, implying $f(r) = 1 - 2cr^2 + O(r^4)$ and hence an approximately de Sitter core with finite central energy density. A common physical motivation for such a de Sitter–like interior comes from semiclassical reasoning: since the areal radius becomes timelike inside the horizon, it is conceivable that—before the classical singularity is reached—there exists a short-distance layer where the dynamics is governed by effective Einstein equations $G_{\mu\nu} = 8\pi G_{\mathrm{N}}\langle T_{\mu\nu}\rangle$, with $\langle T_{\mu\nu}\rangle$ the suitably renormalized stress-energy expectation value. In Schwarzschild-like coordinates, the sign of $\langle T^t{}_t\rangle$ is correlated with the fate of the interior: for $\langle T^t{}_t\rangle < 0$, vacuum-polarization effects can become self-regulatory and lead to a quasilocal mass scaling $M(r) \sim r^3$ at small radii, i.e. to a de Sitter core [4,27]. This perspective is closely related to the limiting-curvature hypothesis, where the cosmological constant sources the transition to a microscopic de Sitter spacetime [58–62].

The Ghosh-Culetu class (3e) can be viewed as a phenomenological representative of a regularization mechanism that is qualitatively distinct from the usual de Sitter–core paradigm. Its defining feature is an exponential suppression of the quasilocal mass at small areal radius, $M(r) \to 0$ as $r \to 0^+$, so that $f(r) = 1 - 2M(r)/r \to 1$ and the interior approaches an asymptotically Minkowski core [33–35,57]. Physically, this realizes singularity resolution by a faster *decoupling* of the central region from the asymptotic mass, leading to a vanishing energy density rather than by replacing the center with a finite-density de Sitter phase. In this sense, (3e) provides a useful test case for assessing which aspects of the inner-horizon dynamics are specific to de Sitter cores and which persist for flat-core regularizations.

The AS-collapse geometry (3f) is not introduced *ad hoc* but arises from a collapse construction of a gravity-matter system within the asymptotic-safety program [37]. In this case, the core is a ball of matter of finite size whose boundary lies inside the CH [37,57,63]. In particular, the antiscreening behavior of Newton's coupling at high density weakens the effective gravitational interaction at short distances and leads to a $M(r) \sim r^3 \log r$ behavior in this limit.

In particular, in the asymptotic-safety program, the scale dependence of the gravitational coupling is inherited from a non-Gaussian fixed point, detected via functional renormalization group techniques. This framework provides a possible nonperturbative ultraviolet completion for gravity-matter systems [64,65], preventing the occurrence of the fatal divergences typical of the perturbative approach. Physically speaking, the presence of a nontrivial fixed point for the dimensionless gravitational coupling g represents an additional "protective" property when in the extreme collapse regime: the *quantum scale symmetry* [66,67]. However, the nonperturbative running of the dimensionful coupling $G(k)$, which gets weaker and eventually vanishes at the fixed point, is usually derived in term of the Euclidean momentum k. In order to obtain the physical varying coupling $G(\epsilon)$ and cosmological constant $\Lambda(\epsilon)$ which enters into the scale-dependent field equations $G_{\mu\nu} = 8\pi G(\epsilon) - \Lambda(\epsilon)g_{\mu\nu}$, with ϵ being the energy-density of the collapsing matter ball, a prescription relating k and ϵ is needed. In the AS-collapse model [37], k was related to a distance scale d interpreted as the proper distance in a spherically symmetric setting, as in [30]: $k \sim 1/d \sim \sqrt{\epsilon}$. Indeed, the analysis in [68] demonstrates that the ultraviolet scaling of the physical Newton constant $G_{\mathrm{N}}(q)$, where q is the external momentum in a graviton-graviton scattering amplitude, is in essence the same as predicted by the renormalized coupling $G(k) = G_{\mathrm{N}}/(1 + G_{\mathrm{N}}k^2/g*)$. Hence the identification $k \sim 1/d$ should capture the qualitative features of the physical flow [69]. This rationale leads to the expression $G(\epsilon) = G_{\mathrm{N}}/(1 + \xi\epsilon)$, and the collapsing matter ball lying inside the CH is asymptotically free in the large-ϵ regime, transitioning into a vacuum-like state of nongravitating particles [57]. Finally, since in the AS-collapse model, G and Λ are uniquely bounded, the former expression implies $\Lambda(\epsilon) = \log(1 + \xi\epsilon)/\xi - \epsilon/(1 + \xi\epsilon)$ [37]. Then, the resolution of the modified field equations for collapsing matter, and the subsequent smooth matching of spacetimes at the boundary of the ball, carry the logarithmic factor all the way to the effective energy-momentum of the surrounding static anisotropic vacuum, thus to $M(r)$ in (3f).

As highlighted in the next subsections, independently of the model origin and of the core type, the CH stability remains a foundational dynamical aspect of regular black holes, which is crucial to address in order to understand the theoretical and phenomenological viability of the nonsingular black-hole physics paradigma.

A. Kinematical origin of the Cauchy horizon instability

We outline the fundamental physical mechanism behind the CH instability in the RN geometry (3a). In Schwarzschild-like coordinates,

$$ds^2 = -f(r)dt^2 + \frac{1}{f(r)}dr^2 + r^2 d\Omega^2, \tag{4}$$

with

$$f(r) = 1 - \frac{2m}{r} + \frac{e^2}{r^2}. \tag{5}$$

Our focus is on spacetimes where $f(r) = 0$ has two solutions $r_+ > r_- > 0$, corresponding to the (outer) event horizon and the (inner) CH. We define the surface gravities

$$\kappa_\pm \equiv \pm \frac{1}{2}\frac{\partial f(r)}{\partial r}\bigg|_{r=r_\pm}, \tag{6}$$

so that $\kappa_\pm > 0$ by definition. The horizons are located at

$$r_\pm = m \pm \sqrt{m^2 - e^2}, \qquad |e| < m, \tag{7}$$

and the surface gravities evaluate to

$$\kappa_\pm = \frac{r_+ - r_-}{2r_\pm^2}. \tag{8}$$

Introducing the tortoise coordinate $r_* = \int dr/f(r)$ and the Eddington-Finkelstein null coordinates

$$\bar{v} = t + r_*, \qquad \bar{u} = t - r_*, \tag{9}$$

one finds that $\bar{u} \to \infty$ at the event horizon. A freely falling observer uses instead a regular retarded time $U_{\mathrm{obs}} = e^{-\kappa_+ \bar{u}}$ and therefore experiences no divergence when crossing the event horizon, while signals sent outward are infinitely redshifted for distant observers.

To extend into the black hole interior one switches to a patch where $u = r_* - t$ and $v = t + r_*$, with $u \in (-\infty, \infty)$ as r ranges between r_+ and r_-. The coordinate singularity at the inner horizon is removed by Kruskal coordinates

$$\kappa_- U = -e^{-\kappa_- u}, \qquad \kappa_- V = -e^{-\kappa_- v}. \tag{10}$$

Near the CH the metric approaches

$$ds^2 \simeq -2dUdV + r^2 d\Omega^2, \tag{11}$$

and the key point is the relation between the exterior advanced time v and the local advanced time V,

$$\Delta V = -e^{-\kappa_- v}\Delta v. \tag{12}$$

Thus, radiation emitted during a finite external interval Δv is received in a vanishingly small interval ΔV as $v \to \infty$: the CH is a surface of *infinite blueshift*, also see Fig. 1 for illustration. This was the basis of Penrose's conjecture that the region beyond the CH is physically unstable [3].

Notably, the Kruskalization is independent of the specific functional form of $M(r)$. Thus, the result based on a purely kinematical rationale extends to regular black holes as well.

B. Backreaction in RN: Poisson-Israel cross-flow

Poisson and Israel incorporated backreaction by modeling the late-time interior as a null cross-flow [4,5] in a RN geometry. In a realistic collapse, ingoing radiation is dominated at late times by the Price tail generated by backscattering in the exterior, while an outgoing component is generated by scattering on the internal potential barrier. In the geometric-optics regime the outflow produced by the collapsing star is integrable and becomes negligible in the corner region relevant for the early portion of the CH [55]. The Poisson-Israel model encodes the remaining cross-flow in the stress tensor

$$T_{\alpha\beta} = \frac{L_{\mathrm{in}}(V)}{4\pi r^2}\partial_\alpha V \partial_\beta V + \frac{L_{\mathrm{out}}(U)}{4\pi r^2}\partial_\alpha U \partial_\beta U. \tag{13}$$

Assuming the late-time ingoing flux decays as a power law in the external advanced time v (Price-type tails), one finds

$$\begin{aligned} L_{\mathrm{in}}(V) &= \frac{dm_{\mathrm{in}}}{dv}\left(\frac{dv}{dV}\right)^2 \\ &= \frac{\beta}{(-\kappa_- V)^2}[-\log(-\kappa_- V)]^{-p}, \end{aligned} \tag{14}$$

so that $L_{\mathrm{in}}(V)$ diverges as $V \to 0^-$. Consequently, the mass function and curvature invariants such as the Coulombian component of the Weyl tensor Ψ_2 diverge and a null (weak) singularity forms at the CH [4,5].

In the remainder of this work, we adopt Ori's simplification of the cross-flow problem, which replaces the continuous outgoing luminosity with a thin outgoing shell. This approximation reduces the dynamics to a tractable system of ordinary differential equations while preserving the essential backreaction mechanism, allowing us to study the dynamics of perturbations beyond the RN case. The physical assumptions and limitations of this approach are discussed explicitly in the next section.

III. ORI MODEL

The Ori model [6] is an analytical framework to study the backreaction associated with the CH instability. It is based on the Poisson-Israel cross-flow picture but approximates the outgoing continuous flux in (13) by an infinitesimally thin null shell,

$$L_{\mathrm{out}}(U) \longrightarrow \delta(U - U_0), \tag{15}$$

so that the interior dynamics becomes a nonlinear ODE problem. This section summarizes the model ingredients needed for our phase-space analysis.

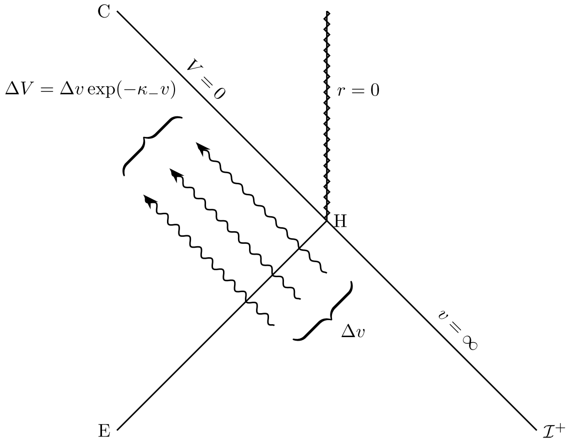

FIG. 1. Radiation falling into a Reissner-Nordström black hole. The light is emitted during a period of external advanced time Δv and an observer inside the hole receives the signals during an interval of internal advanced time ΔV.

We start from a static background geometry and introduce perturbations in the form of null cross-flowing radiation [4,5]. Following [6] the outgoing perturbation is modeled by a spherically symmetric, infinitesimally thin, pressureless null shell Σ located between the event horizon and the CH (Fig. 2). The shell separates spacetime into an inner region $\mathcal{M}_+$ and an outer region $\mathcal{M}_-$. In each region we use ingoing Eddington-Finkelstein coordinates,

$$ds_\pm^2 = -f_\pm(v_\pm, r)dv_\pm^2 + 2dr dv_\pm + r^2 d\Omega^2. \quad (16)$$

The shell trajectory $r = R(v)$ is null, which implies

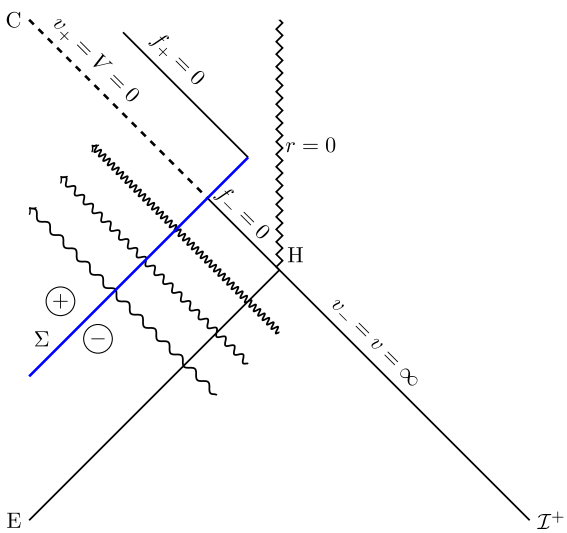

FIG. 2. Penrose diagram illustrating the Ori model for the interior of a Reissner-Nordström black hole [6]. The event horizon (E) and Cauchy horizon (C) meet at the corner H. Outgoing radiation is modeled by a thin shell Σ (blue line) which crosses the Cauchy horizon. A weak singularity forms on the Cauchy horizon in the region $\mathcal{M}_+$ (bold dashed line).

$$f_- dv_- = 2dr = f_+ dv_+. \quad (17)$$

Using $v \equiv v_-$, the shell position evolves according to

$$\frac{\partial R(v)}{\partial v} = \frac{1}{2} f_-(v, r)\bigg|_\Sigma. \quad (18)$$

The remaining ingredient is the relation between the Misner-Sharp masses $M_\pm$ in the two sectors, which follows from the null junction conditions at Σ [70]. Writing Einstein's equations in each region in terms of $M(v, r)$ yields

$$\frac{\partial M(v,r)}{\partial r} = -4\pi r^2 T^v_v, \qquad \frac{\partial M(v,r)}{\partial v} = 4\pi r^2 T^r_v, \quad (19)$$

with $T_{rr} = 0$. Continuity across Σ requires

$$[T_{\mu\nu} s^\mu s^\nu] = 0, \quad (20)$$

where the null generators can be chosen as $s^\mu_\pm = (2/f_\pm, 1, 0, 0)$. Recasting (20) in terms of $M_\pm$ gives

$$\frac{1}{f_+^2} \frac{\partial M_+}{\partial v_+}\bigg|_\Sigma = \frac{1}{f_-^2} \frac{\partial M_-}{\partial v_-}\bigg|_\Sigma. \quad (21)$$

Using (17) this becomes

$$\frac{1}{f_+(v,r)} \frac{\partial M_+(v,r)}{\partial v}\bigg|_\Sigma = F(v), \quad (22)$$

with

$$F(v) \equiv \frac{1}{f_-(v,r)} \frac{\partial M_-(v,r)}{\partial v}\bigg|_\Sigma. \quad (23)$$

Taking M_+ as a function of r and a single parameter $m_+(v)$, Eq. (22) yields

$$\dot{m}_+(v) = \left[\frac{\partial M_+(r, m_+)}{\partial m_+}\right]^{-1} f_+(r, m_+) F(v)\bigg|_\Sigma. \quad (24)$$

Equations (18) and (24) specify the dynamics of the Ori model independently of the specific background geometry. They rely only on: (i) spherical symmetry, (ii) the thin-shell idealization of the outgoing flux, and (iii) the null junction condition (20) derived from general relativity. The model-dependent input enters through the functional form of $M(r)$ listed in (3).

The completion of the model requires specifying the late-time behavior of the ingoing perturbation outside the shell. We parametrize this by prescribing the mass function in $\mathcal{M}_-$ as

$$m_-(v) = m_0 - \frac{\beta}{(v/v_0)^{p-1}}, \qquad p > 1. \tag{25}$$

Here m_0 is the asymptotic mass in $\mathcal{M}_-$ (which coincides with the ADM mass m of the black hole), β sets the amplitude of the perturbation, and v_0 is an arbitrary reference scale (set to one in the sequel). In our normalization dm_-/dv is proportional to the ingoing luminosity through the event horizon; for gravitational perturbations sourced by quadrupolar radiation one typically expects a steep power-law decay and in our explicit examples we will use representative values such as $p = 12$. We use (25) as boundary data at (or just outside) the event horizon: it encodes the late-time inverse power-law tail generated by backscattering in the *exterior* spacetime [71,72]. This is the only place where Price's law enters explicitly: it fixes the amplitude and decay rate of the *ingoing* perturbation that crosses the outer horizon at late advanced times, then propagating toward the *interior*.

The Ori model is designed to capture the late-time approach to the CH in the "corner" region bounded by the event horizon and the early portion of the CH (the neighborhood of the point H in Fig. 2), where $V \to 0^-$ while $U \to -\infty$. In this regime the physical inputs can be motivated by collapse-based analyses [55]. There are two potential sources of *outgoing* radiation inside the horizon:

(a) A *direct* stellar contribution which is bounded in a freely falling frame at the event horizon and, expressed in the Kruskal coordinate adapted to the inner horizon, decays at early retarded times as $T_{UU} \sim -U^{-2(1+\kappa_+/\kappa_-)}$ for $U \to -\infty$ [55]. It therefore satisfies the Raychaudhuri integrability condition ensuring that an early portion of the CH exists and, in particular, it is negligible in the corner region compared to the scattered component [55].

(b) An outgoing stream which comes from the *reflected* flux produced by scattering at the localized potential barrier. In the geometric-optics regime the reflected component inherits an inverse power-law behavior in retarded time, schematically $T_{uu} \propto (-u)^{-p}$, with an amplitude set by an $O(1)$ reflection coefficient [55]. Importantly, in the corner region this scattering should not depend sensitively on how the geometry is regularized at very small r. For the regular black holes considered here, whose exterior is Schwarzschild-like, it is therefore natural to parametrize the reflected outflow by the same Price-type inverse power-law. Thus, in the following we assume that possible different subleading decay rates arising from the regular black-hole geometries can be modeled by adjusting p and/or the functional form of $m_-(v)$: the *approach rate* to the quasifixed points would still be ruled by the forcing term $F(v)$ with the leading order for $m_-(v)$ given by the addendum β/v^{p-1} in (25). Ultimately, such modifications would not hinder the existence of the fixed points themselves, nor would they alter the structure of the phase space.

Finally, the Ori model is not a fully dynamical collapse calculation. Rather, it takes as input an interior geometry specified by $M(r)$ (which, in the regular black-hole cases, already encodes the assumed short-distance modifications) and propagates the late-time tail through the corner region to determine the resulting mass function scaling near the CH. The framework applies as long as a past-complete segment of the CH exists so that the corner-region approximation is meaningful; if the CH terminates at finite U or is eliminated already in the scattering region, the present description ceases to apply.

IV. UNIVERSAL LATE-TIME DYNAMICS

Starting from Eqs. (18) and (22), we now discuss universal features of the dynamics encoded in the Ori model. In order to lighten our notation, derivatives with respect to v are denoted by a dot.

We start with Eq. (18). Once Price's law (25) is adopted, this turns into a first order differential equation for the position of the shell $R(v)$. Obviously, $R(v) = r_-$ is a solution to this equation, since in this case the rhs vanishes due to the horizon condition $f(r_-) = 0$. The dynamics of the shell impacting on the CH can then be studied by adopting the power-law ansatz

$$R(v) = r_- + \frac{1}{v^s}\sum_{n=0}^{\infty}\frac{a_n}{v^n}. \tag{26}$$

Here s is a to-be-determined parameter and the coefficients a_n encode the information on how the shell approaches the horizon. We now demonstrate universality in (26), showing that it is largely independent of the specific form of $f(r)$.

In order to highlight the structure of Eq. (18), we recast the perturbations as

$$m_-(v) = m_0 + \epsilon_1, \qquad R(v) = r_- + \epsilon_2. \tag{27}$$

The explicit form of ϵ_1 and ϵ_2 can be extracted from Eqs. (25) and (26) and read

$$\epsilon_1 = -\frac{\beta}{v^{p-1}}, \qquad \epsilon_2 = \frac{1}{v^s}\sum_{n=0}^{\infty}\frac{a_n}{v^n}. \tag{28}$$

Next, we substitute (27) into (18) and expand to first order in ϵ_i,

$$2\dot{\epsilon}_2 = f_-(r_-, m_0) + \frac{\partial f_-(r_-, m_0)}{\partial m_0}\epsilon_1 + \frac{\partial f_-(r_-, m_0)}{\partial r_-}\epsilon_2 + \mathcal{O}(\epsilon^2). \tag{29}$$

The first term on the rhs vanishes due to the horizon condition. Moreover, the prefactor multiplying ϵ_2 is proportional to the surface gravity (6). Encoding the model-dependent information from the first term by defining

$$\tilde{\beta} \equiv \frac{1}{2} \frac{\partial f_-(r_-, m_0)}{\partial m_0}. \tag{30}$$

Equation (29) takes the form

$$\dot{\epsilon}_2 = \tilde{\beta}\epsilon_1 - \kappa_- \epsilon_2 + \mathcal{O}(\epsilon^2). \tag{31}$$

This equation should be read as an expansion in powers of $1/v$. The parameter s and the coefficients a_n are then found using the Frobenius method. In a nontrivial solution, the leading powers of $1/v$ are provided by the terms proportional to ϵ_1 and ϵ_2. This fixes the free parameter s in Eq. (26) to

$$s = p - 1. \tag{32}$$

Thus the leading term in ϵ_2 follows the same power law as Price's law, *as long as the horizon comes with a nonvanishing surface gravity.* This result is independent of the underlying geometry.

The coefficients a_n are then readily found by solving Eq. (31) order by order in $1/v$. The first few coefficients are

$$a_0 = -\frac{\beta\tilde{\beta}}{\kappa_-}, \tag{33a}$$

$$a_{n+1} = \frac{1}{\kappa_-}(p - 1 + n)a_n, \qquad n < p - 2. \tag{33b}$$

The recursion relation (33b) shows that the timescale associated with the perturbation settling on the CH is set by the surface gravity κ_-. For $n \geq p - 1$ onward, terms quadratic in ϵ start contributing and modifying the linear relation (33b). While it is possible to work out these contributions systematically, this is not needed when discussing the late-time behavior of the model analytically. Moreover, Price's law contains the leading fall-off behavior and subleading terms (associated with higher-order multipole moments in the perturbations) may modify ϵ_1 at subleading orders. Therefore, only the lowest order terms in (33) are robust with respect to these additional corrections.

In the next step, we focus on the late-time behavior entailed by Eq. (24). In order to aid the discussion, we introduce the abbreviation

$$g(r, m_+) \equiv \left[\frac{\partial M_+(r, m_+)}{\partial m_+}\right]^{-1}\Bigg|_{\Sigma}. \tag{34}$$

The expression (24) allows to distinguish several cases. First, the rhs can be linear in m_+. This happens if the Misner-Sharp mass is a linear function of the asymptotic mass and applies to the RN black hole (3a) and the regular Bardeen black hole (3b). This leads to a single repulsive quasifixed point and to the standard mass-inflation instability where the Misner-Sharp mass grows exponentially in v, cf. Eq. (74).

Second, the rhs may have nontrivial roots $m_{+,*}$ where

$$g(r_-, m_{+,*}) = 0, \tag{35}$$

as in the case of the black holes (3c)–(3f). Clearly, $m_{+,*}$ is a solution of (24) if the equation its evaluated at the CH. This gives rise, in the dynamics of the system $[R(v), m_+(v)]$, to additional quasifixed points located at $(r_-, m_{+,*})$. Notably, it is an attractive quasifixed point that underlies the late-time attractors discovered in [50]. Indeed, differently from the fixed point corresponding to the trivial root, the ones corresponding to the additional roots can be attractive.

We proceed by determining the generic late-time behavior induced by these attractors, indicating a quantity that is evaluated at the attractor by $*$. Furthermore, we make the generic assumptions that, first, the metric functions are continuous and sufficiently differentiable everywhere, second, that $f_+(r_-, m_{+,*}) \equiv f_{+,*}$ takes a finite and nonvanishing value, and, third, that

$$\lim_{v\to\infty} F(v) \equiv F_* \tag{36}$$

approaches a finite value asymptotically. Finally, we assume that the late-time dynamics of $m_+(v)$ can be captured by the Frobenius ansatz

$$m_+(v) = m_* + \frac{1}{v^t}\sum_{n=0} \frac{b_n}{v^n}, \tag{37}$$

where t and b_n are coefficients to be determined. Following the notation introduced in Eq. (31), we denote the perturbations around the attractor by

$$\epsilon_3 \equiv \frac{1}{v^t}\sum_{n=0} \frac{b_n}{v^n}. \tag{38}$$

We proceed by expanding g around the attractor

$$g[R(v), m_+(v)] \simeq g(r_-, m_*) + \left(\frac{\partial g}{\partial r}\right)_* \epsilon_2 + \left(\frac{\partial g}{\partial m_+}\right)_* \epsilon_3 + \mathcal{O}(\epsilon^2). \tag{39}$$

The condition (35) ensures that the first term in the expansion vanishes. Equation (24) then states that the late-time behavior of the system is captured by

$$\dot{\epsilon}_3 = \left[\left(\frac{\partial g}{\partial r}\right)_* \epsilon_2 + \left(\frac{\partial g}{\partial m_+}\right)_* \epsilon_3\right] f_{+,*} F_*. \tag{40}$$

Remarkably, the subleading terms in f_+ and $F(v)$ do not play a role. The fall-off of the lhs is then subleading to the fall-off of the rhs. Thus, for a consistent solution, the leading terms in the straight bracket have to vanish. This fixes

$$t = p - 1 \tag{41}$$

and

$$b_0 = -\left(\frac{\partial g}{\partial m_+}\right)_*^{-1} \left(\frac{\partial g}{\partial r}\right)_* a_0. \tag{42}$$

The coefficient b_1 is then fixed from the order $1/v^p$ in the expansion

$$b_1 = -\left[\frac{(p-1)b_0}{f_{+,*}F_*} + \left(\frac{\partial g}{\partial r}\right)_* a_1\right] \left(\frac{\partial g}{\partial m_+}\right)_*^{-1}. \tag{43}$$

Notably, subleading corrections to F_* and $f_{+,*}$ do not enter into b_1. These are needed to determine b_2 only. The reason is that these terms are multiplied by the equation determining b_0 and therefore drop out of (43).

Based on this analysis, we arrive at the following conclusion. Equation (43) is inhomogeneous in the sense that it contains extra contributions which are not generated by the expansion of g. As a consequence

$$g \simeq -\frac{p-1}{f_{+,*}F_*} \frac{b_0}{v^p}. \tag{44}$$

This scaling behavior is dictated by the structure of Eq. (24) and hinges on very few generic assumptions only. Notably, the factor g also appears in M_+. In this way, the result (44) sets the late-time behavior of the Misner-Sharp mass evaluated at the position of the shell,

$$M_+(v) = M_+[R(v), m_+(v)], \tag{45}$$

when approaching the attractor.

At this point, we established that the scaling of g related to the late-time attractor $m_{+,*}$ is rather generic. A way to avoid this conclusion is to violate one of the assumptions underlying its derivation. For example, the Dymnikova black hole (3d), the Ghosh-Culetu geometry (3e), and the AS-collapse model (3f) violate the fact that $f_{+,*}$ is finite. Thus, in these cases, the dynamics close to the attractive fixed points cannot be described by (44) and the ansatz (37). In addition, as we will see in the next section, the geometries (3d) and (3e) give rise to a discontinuity in $\dot{m}_+$, as its $m_+ \to 0$ limit differs when taken from above and below.[3] This suggests that the models (3d)–(3f) could give rise to new scaling behaviors, different from the one induced by (44). This will be investigated on a case-by-case basis.

V. REGULAR BLACK HOLES (IN)STABILITY

Upon discussing general features of the dynamics encoded in the Ori model, we illustrate these features for the specific examples introduced in Eq. (3). We start by analyzing the phase space of the solutions in Sec. V A. Analytic results on the late-time attractor are collected in Sec. V B and we verify these features at the level of numerical solutions in Sec. V C. Section V D then briefly comments on the strength of the singularity building up at the CH. The results of this section are conveniently summarized in Table II.

A. Phase space

As we demonstrated in Sec. IV, the impact of the shell on the CH is independent of the specific features of the geometry. Differences in the stability of the horizon arise from the dynamics of $m_+(v)$. In the following, we discuss the key properties of these equations based on the phase space diagrams shown in Figs. 3 and 6. The parameters used in each geometry are listed in Table I. In particular, we have fixed the mass in Price's law to $m_0 = 1$ and adjusted the free parameters in such a way that the surface gravity κ_-, setting the time-scale of the process, is $\kappa_- = 1$ in all cases. In all cases we highlight the values $m_{+,*}$ of the attractive (repulsive) quasifixed points as gray (black) horizontal lines. The stream plots are then generated at a fixed instance of time v_{section}. Throughout the discussion, we color-code streams repelled by a quasifixed point in red, trajectories ultimately ending at an attractive quasifixed point in green, and solutions terminating at a finite value v in brown.

Bardeen black holes. The Bardeen geometry (3b) yields the simplest phase-space structure. Substituting (3b) into (24) gives

$$\dot{m}_+ = \frac{1}{R^3}[(R^2 + a^2)^{3/2} - 2m_+R^2]F(v), \tag{46}$$

with

[3]We stress that this discontinuity is not related to the thin-shell approximation. It is a feature of the profile $M(r)$ determining the regular black hole geometry. Even if the description in terms of the auxiliary variable m_+ might lead one to think otherwise, the asymptotic behavior of the mass function M_+ is encoded in $M(r)$ and should be independent from the nature (continuous or discrete) of the perturbative fluxes, provided that they make up a cross-flow.

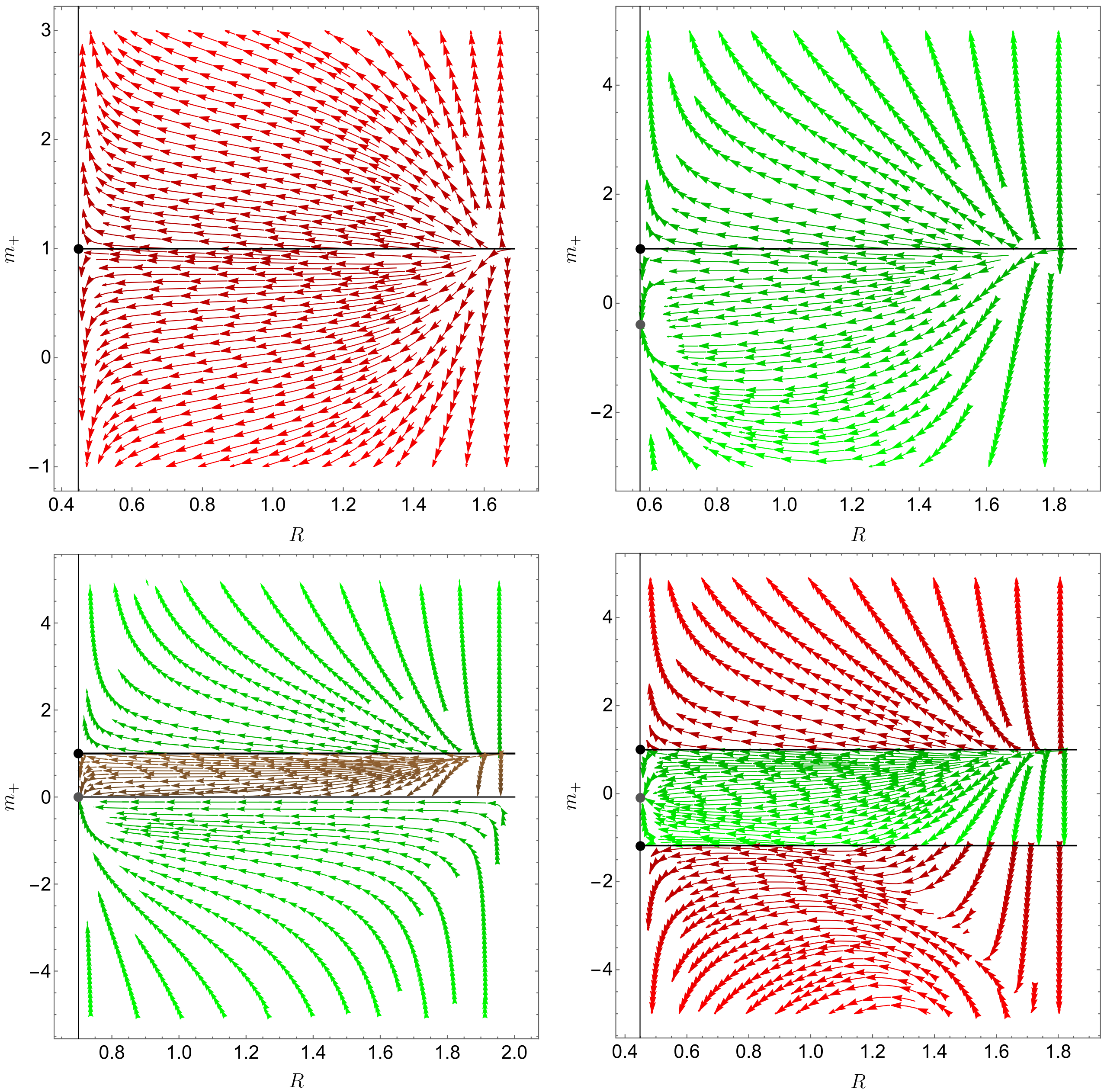

FIG. 3. Illustration of the dynamics arising from the Ori model for the Bardeen geometry (top left), the Hayward geometry (top right), the Dymnikova geometry (bottom left), and the AS-collapse (bottom right). The CH is located at the black vertical line. The position of the attractive (repulsive) quasifixed points $m_{+,*}$ are marked with gray (black) dots and are extended by horizontal lines. The stream lines are indicative for the phases encountered in the models where flows attracted to (repelled by) a quasifixed point are indicated in green (red). In addition, the Dymnikova geometry gives rise to an additional phase (brown) where the solutions terminate at the discontinuity $m_+ = 0$ at a finite value v.

$$F(v) = \frac{R^3}{(R^2+a^2)^{3/2} - 2m_- R^2} \frac{(p-1)\beta}{v^p}. \tag{47}$$

Since the rhs of (46) is linear in m_+, there is a single quasifixed point obtained by evaluating at $R = r_-$,

$$m_{+,*}^{\mathrm{rep}} = \frac{1}{2r_-^2}(r_-^2 + a^2)^{3/2}. \tag{48}$$

The stream plot in the top-left panel of Fig. 3 shows that this quasifixed point is repulsive. Consequently $m_+(v)$ is driven away from $m_{+,*}^{\mathrm{rep}}$ and diverges as $v \to \infty$,

$$\lim_{v\to\infty} m_+(v) = \pm\infty. \tag{49}$$

In this model the divergence of m_+ corresponds to the standard mass-inflation instability discussed in the next

TABLE I. Settings used for generating the stream plots illustrating the phase space dynamics in Figs. 3 and 6.

Solution	Parameter	r_-	r_+	κ_-	$m^{\text{rep}}_{+,*}$	$m^{\text{att}}_{+,*}$	$m^{\text{rep}}_{+,*}$	m_0	β	p	v_{section}
Bardeen	$a = 0.586$	0.447	1.686	1	1	Not applicable	Not applicable	1	1	12	1.7
Hayward	$l = 0.483$	0.571	1.866	1	1	-0.4	Not applicable	1	1	12	1.55
Dymnikova	$\gamma = 0.892$	0.700	2.000	1	1	0	Not applicable	1	1	12	1.5
Ghosh-Culetu	$\alpha = 1.110$	0.359	1.193	1	1	0	Not applicable	1	1	12	1.9
AS-collapse	$\xi = 0.167$	0.448	1.858	1	1	-0.09	-1.18	1	1	12	1.5

subsection. Notably, the RN geometry (3a) leads to the same qualitative phase-space structure, so we do not discuss it separately.

Hayward black holes. For the Hayward geometry (3c), evaluating (24) yields

$$\dot{m}_+ = \frac{[R^3 - 2(R^2 - l^2)m_+](R^3 + 2l^2 m_+)}{R^6} F(v), \qquad (50)$$

with

$$F(v) = \frac{R^6}{(R^3 + 2l^2 m_-)[R^3 - 2m_-(R^2 - l^2)]} \frac{(p-1)\beta}{v^p}. \qquad (51)$$

Here the rhs is quadratic in m_+, implying two quasifixed points obtained at $R = r_-$,

$$m^{\text{rep}}_{+,*} = \frac{r_-^3}{2(r_-^2 - l^2)} > 0, \qquad (52a)$$

$$m^{\text{att}}_{+,*} = -\frac{r_-^3}{2l^2} < 0. \qquad (52b)$$

The phase portrait in the top-right panel of Fig. 3 shows that $m^{\text{rep}}_{+,*}$ is repulsive while $m^{\text{att}}_{+,*}$ acts as a late-time attractor.

Two clarifications are important for the physical interpretation. First, m_+ is an auxiliary variable labeling the interior branch across the outgoing shell in Ori's construction. In particular, negative values of m_+ do *not* imply a negative ADM mass at infinity (which is fixed by the exterior and equals m_0), and the relevant physical diagnostics are the reconstructed Misner-Sharp mass $M_+(v) = M[R(v), m_+(v)]$ and curvature invariants. Second, the quadratic structure of (50) implies that some trajectories reach $m_+(v) = +\infty$ at a finite advanced time v. This blowup is not a physical divergence: the Misner-Sharp mass (3c) remains finite and continuous in the limit $m \to \pm\infty$. Therefore the ODE flow can be continued past $m_+ = \pm\infty$ by compactifying the m_+ direction. In this sense, trajectories that "leave" at $m_+ = +\infty$ reenter at $m_+ = -\infty$, and all solutions ultimately reach the attractor (52b). Formally, this continuation is implemented by changing to a new dynamical variable which maps infinity to a finite value, e.g., by studying the dynamics in terms of $1/m_+(v)$. The presence of this feature regarding the topology of the flow is indicated—for a given geometry—in the column "Extendability" of Table II.

TABLE II. Summary of the key results found in Sec. V. The second column indicates whether solutions reaching $m_+ = \pm\infty$ at finite v can be continued by a reparametrization of m_+ ("extendable") or whether the blowup corresponds to a genuine boundary of the flow ("nonextendable"). The asymptotic scaling of the Misner-Sharp mass is summarized in the column "$M_+(v)$" while the columns "$K_+(v)$," "$C^2_+(v)$," and "$\Psi_{2+}(v)$" give the asymptotics of the Kretschmann scalar, the square of the Weyl-tensor and the Coulomb-component of the Weyl-tensor. All singularities are weak in the Tipler sense. Polynomial growths of the curvature invariants furthermore implies that they are also weak in the Królak sense.

Solution	Extendability		$M_+(v)$	$K_+(v)$	$C^2_+(v)$	$\Psi_{2+}(v)$
RN, Bardeen	Nonextendable		$\propto \pm v^{-p} e^{\kappa_- v}$	$\propto v^{-2p} e^{2\kappa_- v}$	$\propto v^{-2p} e^{2\kappa_- v}$	$\propto \pm v^{-p} e^{\kappa_- v}$
Hayward	Extendable		$\propto v^p$	$\propto v^{6p}$	$\propto v^{6p}$	$\propto -v^{3p}$
Dymnikova	Extendable	Case I:	$\propto v^{-(p+1)} e^{\kappa_- v}$	$\propto v^{-2(p-1)} e^{2\kappa_- v}$	$\propto v^{-2(p-1)} e^{2\kappa_- v}$	$\propto -v^{-(p-1)} e^{\kappa_- v}$
		Case II:	$M_+(v_*) \to 0^+$	...	...	...
Ghosh-Culetu	Nonextendable	Case I:	$\propto \pm v^{-p} e^{\kappa_- v}$	$\propto v^{-2p} e^{2\kappa_- v}$	$\propto v^{-2p} e^{2\kappa_- v}$	$\propto \mp v^{-p} e^{\kappa_- v}$
		Case II:	$M_+(v_*) \to 0^+$	...	...	...
		Case III:	$\propto -v^{-(p+1)} e^{\kappa_- v}$	$\propto v^{-2(p-1)} e^{2\kappa_- v}$	$\propto v^{-2(p-1)} e^{2\kappa_- v}$	$\propto v^{-(p-1)} e^{\kappa_- v}$
AS-collapse	Nonextendable	Case I:	$\propto v^{-p} e^{\kappa_- v}$	$\propto v^{-2p} e^{2\kappa_- v}$	$\propto v^0$	$\propto v^0$
		Case II:	$\propto -\log v^p$	$\propto v^{4p}$	$\propto v^{4p}$	$\propto v^{2p}$

Dymnikova black holes. The evaluation of (24) for the Dymnnikova black hole (3d)leads to

$$\dot{m}_+(v) = \frac{\gamma^2 m_+}{R} \frac{[R - 2m_+(1 - e^{-\frac{R^3}{\gamma^2 m_+}})]}{[\gamma^2 m_+ - e^{-\frac{R^3}{\gamma^2 m_+}}(R^3 + \gamma^2 m_+)]} F(v) \tag{53}$$

with

$$F(v) = \frac{R}{\gamma^2 m_-} \frac{1}{R - 2m_-(1 - e^{-\frac{R^3}{\gamma^2 m_-}})} \times [\gamma^2 m_- - e^{-\frac{R^3}{\gamma^2 m_-}}(R^3 + \gamma^2 m_-)] \frac{(p-1)\beta}{v^p}. \tag{54}$$

We proceed by finding the quasifixed points of Eq. (53). Again there are two roots where the rhs vanishes. The first root arises as the solution of the transcendental equation,

$$r_- - 2m_{+,*}^{\text{rep}}\left(1 - e^{-\frac{r_-^3}{\gamma^2 m_{+,*}^{\text{rep}}}}\right) = 0. \tag{55}$$

Since $r_- > 0$ this root is located at $m_{+,*}^{\text{rep}} > 0$. The repulsive property of this quasifixed point is readily deduced from the phase diagram in the left-bottom panel of Fig. 3. In addition, there is the attractor

$$m_{+,*}^{\text{att}} = 0. \tag{56}$$

Again, the Misner-Sharp mass (3d) is finite and continuous for $m \to \pm\infty$, so solutions can be continued through the finite-v blowup of the parameter m_+ by a compactification of the m_+ direction. As in the Hayward case, we again encounter the cylindrical structure of the phase space.

The Dymnikova geometry gives rise to a qualitative new feature though. In this case the Misner-Sharp mass (3d) posses a discontinuity at $m = 0$,

$$\lim_{m\to 0^+} M(r) = 0, \qquad \lim_{m\to 0^-} M(r) = +\infty. \tag{57}$$

This discontinuity propagates into the rhs of Eq. (53) where

$$\lim_{m_+\to 0^+} \dot{m}_+(v) = F(v), \qquad \lim_{m_+\to 0^-} \dot{m}_+(v) = 0. \tag{58}$$

This has the consequence that solutions cannot reach from above $m_+(v) = 0$. In terms of the phase space $[R(v), m_+(v)]$ this entails that there is a new class of solutions which terminate at finite v where the discontinuity realizes. These solutions correspond to the brown cluster in the left-bottom panel of Fig. 3.

Ghosh-Culetu black holes. Equation (24) evaluated for the Ghosh-Culetu geometry (3e) is

$$\dot{m}_+(v) = \frac{m_+(2e^{\frac{\alpha^2}{2Rm_+}}R - 4m_+)}{\alpha^2 + 2Rm_+} F(v), \tag{59}$$

with

$$F(v) = \frac{\alpha^2 + 2Rm_-}{m_-(2e^{\frac{\alpha^2}{2Rm_-}}R - 4m_-)} \frac{(p-1)\beta}{v^p}. \tag{60}$$

The trivial repulsive fixed point $m_{+,*}^{\text{rep}} > 0$ is determined by the root of the trascendental equation

$$2e^{\frac{\alpha^2}{2r_- m_{+,*}^{\text{rep}}}} r_- - 4m_{+,*}^{\text{rep}} = 0, \tag{61}$$

while the attractor is

$$m_{+,*}^{\text{att}} = 0, \tag{62}$$

and, similarly to the Dymnikova case, is characterized by the discontinuity

$$\lim_{m_+\to 0^+} \dot{m}_+(v) = -\infty, \qquad \lim_{m_+\to 0^-} \dot{m}_+(v) = 0. \tag{63}$$

The latter is inherited from

$$\lim_{m\to 0^+} M(r) = 0, \qquad \lim_{m\to 0^-} M(r) = -\infty. \tag{64}$$

The cluster leading to discontinuous trajectories is labeled in brown in Fig. 6 of Appendix B.

The structure of the phase space is further shaped by a pole in (59), at

$$m_+ = -\frac{\alpha^2}{2R}, \tag{65}$$

which separates the $m_+ < 0$ region into dynamically disconnected sectors and gives rise to an additional family of trajectories (a fourth extra "cluster" in Fig. 6). The change of sign occurring at the curve $m_+(v_i) = -\alpha^2/2R(v_i)$ determines a boundary between trajectories sinking in $m_{+,*}^{\text{att}}$ from below and the ones repelled toward minus infinity.

Finally, since $M(r) \sim m$ for $m \to \pm\infty$, the blowup of m_+ corresponds to a genuine boundary of the flow in this model (no extendability through $m_+ = \pm\infty$, as in the RN and Bardeen cases).

Black holes from the AS-collapse. Equation (24) evaluated for the AS-collapse (3f) is

$$\dot{m}_+(v) = \left[1 - \frac{R^2}{6\xi}\log\left(1 + \frac{6\xi m_+}{R^3}\right)^2\right]\left(1 + \frac{6\xi m_+}{R^3}\right) F(v), \tag{66}$$

with

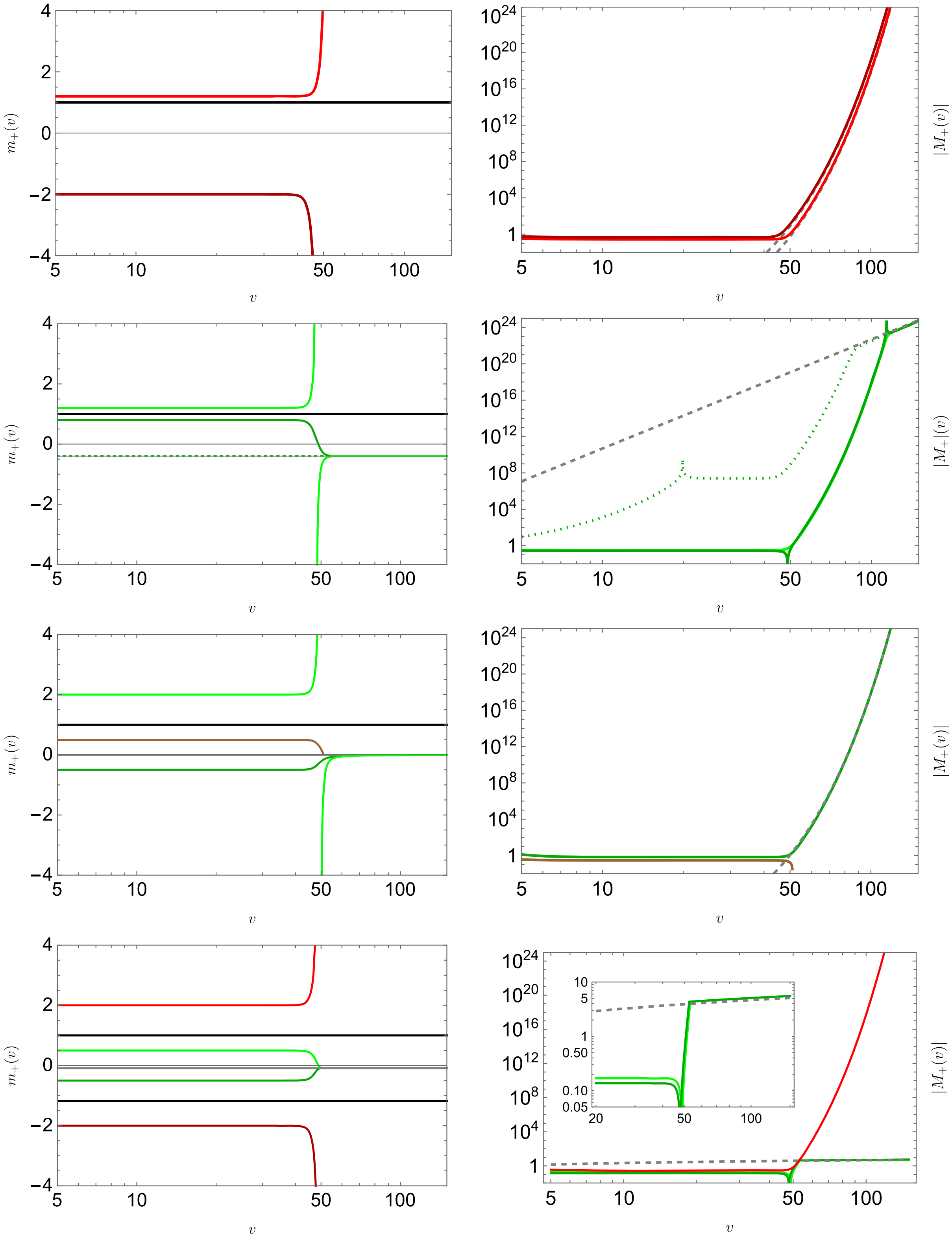

FIG. 4. Illustration of the dynamics found for the Orimodel for various regular black-hole geometries. From top to bottom the geometry is given by the Bardeen black hole (3b), the Hayward geometry (3c), the Dymnikova black hole (3d), and the AS collapse (3f), respectively. The left column shows the mass-function $m_+(v)$ while the right column displays the absolute value of the Misner-Sharp mass $M_+(v)$ reconstructed from the numerical solutions for $\{R(v), m_+(v)\}$ on a double-logarithmic scale. The attractive (repulsive) quasifixed points for $m_{+,*}$ are given by gray (black) horizontal lines while the late-time attractors for $M_+(v)$ constructed in Sec. V B are superimposed as gray dashed lines. See the main text for further details.

$$F(v) = \frac{1}{\left[1 - \frac{R^2}{6\xi}\log\left(1 + \frac{6\xi m_-}{R^3}\right)^2\right]\left(1 + \frac{6\xi m_-}{R^3}\right)} \frac{(p-1)\beta}{v^p}. \quad (67)$$

The search for quasifixed points reveals that there are three values where the rhs of (66) vanishes when evaluated at $R = r_-$,

$$m_{+,*}^{\mathrm{rep}} = -\frac{r_-^3}{6\xi}\left(1 - e^{\frac{3\xi}{r_-^2}}\right) > 0, \quad (68a)$$

$$m_{+,*}^{\mathrm{att}} = -\frac{r_-^3}{6\xi} < 0, \quad (68b)$$

$$m_{+,*}^{\mathrm{rep}} = -\frac{r_-^3}{6\xi}\left(1 + e^{\frac{3\xi}{r_-^2}}\right) < 0. \quad (68c)$$

Equation (68), and the phase space diagram in the bottom-right panel of Fig. 3, show that the repulsive quasifixed points sandwich the attractor. As a consequence, only initial data in the wedge between the two repulsive quasifixed points are captured by the attractive one, while the rest of the trajectories diverge as the shell settles onto the CH. The blowup of m_+ here corresponds to a genuine boundary of the flow: a continuation through $m_+ = \pm\infty$ is not available, and the phase space is globally nonextendable.

B. Quasifixed points: Analytic results

In the previous section, we identified several late-time attractors for the various regular black-hole geometries studied in this work. The goal of this section is to obtain analytic results for the scaling behavior associated with these attractors. Throughout this section, we will use the $\simeq$ symbol to stress that an expression corresponds to an asymptotic expansion at large values of v and it is tacitly understood that subleading corrections to the expansion are not displayed.

We start with the late-time dynamics of the shell impacting on the CH. Adapting the general analysis of Sec. IV to the geometries (3), one readily finds that the late-time dynamics of $R(v)$ is model independent to a large extent. The terms relevant to the construction of the Misner-Sharp mass read

$$R(v) - r_- \simeq \frac{1}{v^{p-1}} a_0 \left[1 + \frac{p-1}{\kappa_- v} + \frac{p(p-1)}{\kappa_-^2 v^2}\right]. \quad (69)$$

The constants a_0 capture the information on the specific geometry. Their explicit values are readily obtained from evaluating Eq. (33a) and read

$$\text{Bardeen:}\ a_0 = \frac{\beta}{\kappa_-}\frac{r_-^2}{(a^2 + r_-^2)^{3/2}}, \quad (70a)$$

$$\text{Hayward:}\ a_0 = \frac{\beta}{\kappa_-}\frac{r_-}{4m_0^2}, \quad (70b)$$

$$\text{Dymnikova:}\ a_0 = \frac{\beta}{\kappa_-}\frac{(r_-^3 + m_0\gamma^2 - 2m_0 r_-^2)}{2\gamma^2 m_0^2}, \quad (70c)$$

$$\text{Ghosh-Culetu:}\ a_0 = \frac{\beta}{\kappa_-}\frac{\alpha^2 + 2m_0 r_-}{4m_0^2 r_-}, \quad (70d)$$

$$\text{AS-collapse:}\ a_0 = \frac{\beta}{\kappa_-}\frac{1}{r_-}\left(1 + \frac{6m_0\xi}{r_-^3}\right)^{-1}. \quad (70e)$$

Analyzing the dynamics related to $m_+(v)$ then requires the late-time asymptotics of $F(v)$. Retaining terms up to a_2 in the asymptotic expansion of $R(v)$, one finds that

$$F(v) \simeq -\frac{r_-}{2}\left(\kappa_- - \frac{p}{v}\right). \quad (71)$$

The relative factor between the terms appearing in the brackets are set by the recursion relation (33b). Remarkably, this result holds for all geometries in this section. The resulting consequences for the Misner-Sharp mass depend on the chosen geometry, though, and are discussed on a case by case basis.

Bardeen black holes. The repulsive nature of the quasifixed point (48) indicates that, asymptotically, m_+ will be large. Thus, we can approximate (46) by retaining the terms proportional to m_+ on its rhs only. Substituting the asymptotic expansion (71) then yields the following approximation, capturing the late-time behavior of $m_+(v)$,

$$\dot{m}_+ \simeq m_+\left(\kappa_- - \frac{p}{v}\right). \quad (72)$$

This equation is readily integrated, yielding

$$m_+(v) \simeq \pm c v^{-p} e^{\kappa_- v}. \quad (73)$$

Here $c > 0$ is an integration constant. Note that the result applies universally for flows being repelled by $m_{+,*}^{\mathrm{rep}}$ with the signs in (73) capturing the limits $m_+(v) = \pm\infty$. Equation (73) allows to reconstruct the asymptotics of the Misner-Sharp mass, establishing that

$$M_+^{\mathrm{rep}}(v) \simeq \pm \frac{r_-^3}{(r_-^2 + a^2)^{3/2}} c v^{-p} e^{\kappa_- v}. \quad (74)$$

Hence $M_+(v)$ grows exponentially and we establish that the repulsive quasifixed point yields the standard result of eternal mass inflation. Again, the result (73) also holds for the RN geometry.

Hayward black holes. The Hayward geometry is a prototypical realization of the generic scaling behavior discussed in Sec. IV. Its late-time dynamics is governed by the quasifixed point (52b), which acts as a global attractor.

The scaling behavior of $m_+(v)$ is readily obtained from the Frobenius analysis. Including all terms relevant for the reconstruction of $M_+(v)$ one has

$$m_+(v) - m^{\text{att}}_{+,*} \simeq -\frac{3\beta r_-^3}{8l^2 m_0^2 \kappa_-}\frac{1}{v^{p-1}}\left[1 + \frac{2(p-1)}{\kappa_- v}\right]. \tag{75}$$

Note that there is no free coefficient in the expansion. Thus the attractor fixes the late-time behavior completely. Substituting the asymptotic expansions (69) and (75) into the Misner-Sharp mass (3c) and taking into account the cancellation of the leading terms appearing in the denominator finally yields

$$M^{\text{att}}_+(v) \simeq \frac{2}{3}\frac{r_-^3 m_0^2 \kappa_-^2}{\beta(p-1)l^2}v^p. \tag{76}$$

Notably, $M_+(v)$ no longer grows exponentially in v and follows a power-law behavior. This is the imprint of the attractor discovered in [50,73]. In combination with the phase-space analysis, this entails that any initial condition will ultimately follow this power law.

Dymnikova black holes. Case I: The late-time attractor shown in the bottom-left diagram of Fig. 3 is characterized by the limit $m_+ \to 0^-$. In this limit, the rhs of Eq. (53) is dominated by the exponential terms. Retaining these contributions only, the exponentials in the numerator and denominator cancel. Substituting the late-time behavior of $F(v)$ given by (71) then leads to the following differential equation capturing the late-time behavior of $m_+(v)$ close to the one-sided attractor

$$\dot{m}_+ \simeq \frac{\gamma^2\kappa_-}{r_-^3}\left(1 - \frac{p}{\kappa_- v}\right)m_+^2. \tag{77}$$

This equation is readily integrated, yielding

$$m_+(v) \simeq -\frac{r_-^3}{\gamma^2}(\kappa_- v - p\log v + \bar{c})^{-1}, \tag{78}$$

where $\bar{c}$ is an integration constant. Substituting this result into the Misner-Sharp mass (3d) then yields

$$M^{\text{att}}_+(v) \simeq \frac{r_-^3}{\gamma^2\kappa_-}c v^{-(p+1)}e^{\kappa_- v}, \tag{79}$$

with $c > 0$ always.

In principle, the dependence on c could be eliminated by implementing a nonpolynomial Frobenius ansatz in solving (53) (since $f_{+,*} \to \infty$ the standard procedure based on the polynomial ansatz (37) cannot be applied). However, as we have just shown, solving the approximate Eq. (77) is sufficient to reveal that the late-time attractor (56) induces

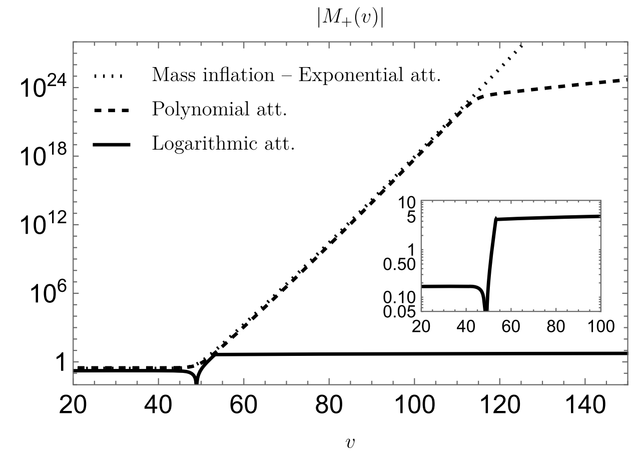

FIG. 5. Comparison, in a log-plot, between the relevant different dynamics found within the phase space of the Ori model for regular black-hole geometries. The examples cover eternal mass-inflation in the Bardeen model (black-dotted line), the polynomial attractor realized by the Hayward model (black-dashed) and the logarithmic attractor (68b) of the AS-collapse model (black-solid). While solutions still undergo transient mass inflation before reaching the polynomial attractor, this feature is absent in the case of the logarithmic attractor.

an exponential scaling in the Misner-Sharp mass. The dynamics is governed by an "*exponential attractor*," which ultimately mimics the phenomenon of mass inflation. Thus, the existence of an attractive quasifixed point does not, by itself, guarantee the absence of an exponential instability. In order to suppress (or tame) this instability, the rhs of Eq. (24) must contain a suitable nonlinearity in m_+, whose origin is related to the functional form of $M(r)$. Finally, the shift observed in the exponent of the subleading power-law corrections in (79) arises from the multiplicative factor m that appears in the Misner-Sharp mass definition (3d).

Case II: Determining the fate of the trajectories terminating at $m_+(v_*) = 0^+$ is beyond the scope of the Ori model. Thus we will not discuss this case and just add it to Table II for the sake of completeness.

Ghosh-Culetu black holes. Case I: The initial conditions corresponding to $m_+(v_i) > m^{\text{rep}}_{+,*}$ or $m_+(v_i) < -\alpha^2/[2R(v_i)]$ lead the stream toward large values of m_+, respectively, positive or negative. Consequently, we can approximate Eq. (59) as in the Bardeen case of Eq. (72). For the Misner-Sharp, this leads to the standard mass-inflation solution

$$M^{\text{rep}}_+(v) \simeq \pm c v^{-p} e^{\kappa_- v}, \tag{80}$$

with $c > 0$.

Case II: Again, determining the fate of the trajectories terminating at $m_+(v_*) = 0^+$ is beyond the scope of the Ori model and we just add this possibility to Table II for completeness.

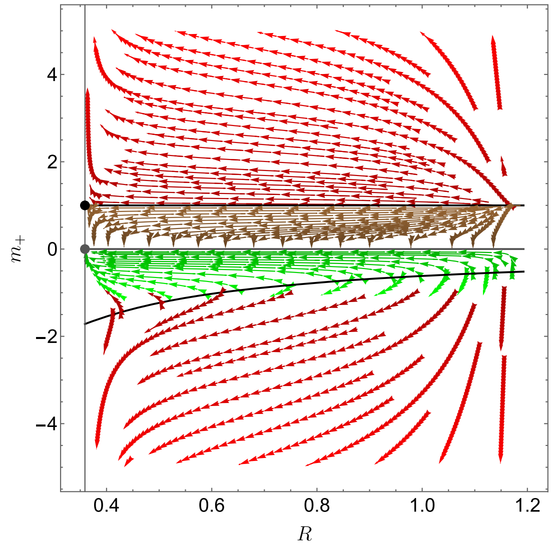

FIG. 6. Phase space for the Ghosh-Culetu geometry. The poles $m_+(v_i) = -\alpha^2/R(v_i)$ are indicated by the black curve. The free parameters of the background geometry are set as indicated in Table I.

Case III: For initial conditions satisfying $-\alpha^2/[2R(v_i)] < m_+(v_i) < m^{\rm rep}_{+,*}$, the dynamics is governed by the one-sided attractor $m^{\rm att}_{+,*} = 0$ (see Fig. 6). For $m_+ \to 0^-$, the equation of motion approximates to

$$\dot m_+ \simeq \frac{2r_-\kappa_-}{\alpha^2}\left(1 - \frac{p}{\kappa_- v}\right) m_+^2, \tag{81}$$

whose integration yields

$$m_+(v) \simeq -\alpha^2(2r_-\kappa_- v - 2p\log v + \bar c\alpha^2)^{-1}. \tag{82}$$

Thus, the reconstructed growth of $M_+(v)$ induced by $m^{\rm att}_{+,*}$ can be obtained without relying to a Frobenius ansatz, and reads

$$M^{\rm att}_+(v) \simeq -\frac{\alpha^2}{r_-\kappa_-} c v^{-(p+1)} e^{\kappa_- v}, \tag{83}$$

with $c > 0$. Considerations similar to those on the attractor of the Dymnikova geometry apply.

Black holes from the AS collapse. Case I: The repulsive flows associated with the quasifixed points (68a) and (68c) lead to solutions where $m_+(v) \to \pm\infty$, respectively. To obtain the related scaling, we start from (66) and consider the regime where $m_+ \gg 1$. Retaining the leading and subleading terms contributed by $F(v)$, the asymptotic behavior of these solutions at large values m_+ is captured by

$$\dot m_+ \simeq \frac{\kappa_-}{2}\log(m_+^2) m_+ \left(1 - \frac{p}{\kappa_- v}\right). \tag{84}$$

This approximation is at the same level as Eq. (72), capturing the mass-inflation instability in the Bardeen geometry. Notably, Eq. (84) admits an analytic solution

$$m_+(v) \simeq \pm\exp\left(c v^{-p} e^{\kappa_- v}\right), \tag{85}$$

where $c > 0$ is an integration constant. Reconstructing the Misner-Sharp mass based on (85) yields

$$M^{\rm rep}_+ \simeq \frac{r_-^3}{6\xi} c v^{-p} e^{\kappa_- v}. \tag{86}$$

Remarkably, both repulsive quasifixed points lead to the standard mass-inflation instability. Since the Misner-Sharp mass contains the square of $m_+(v)$ only, the result (86) applies to both cases $m_+(v) = \pm\infty$.

Case II: The solutions whose late-time behavior is controlled by the attractive quasifixed point (68b) feature a peculiar logarithmic growth of $M_+(v)$. For this reason, we refer to this fixed point as *“logarithmic attractor.”* The derivation of its scaling is slightly more complicated and details are relegated to Appendix C. In summary, we employ two subsequent changes of variable, $m_+ \mapsto x$ and $x \mapsto y$, defined, respectively, by (C2) and (C7), and a suitable Frobenius ansatz, as in (C11). This is necessary because the singular point of the differential equation (66) is described by a nonpolynomial term, and it holds $f_{+,*} \to \infty$. Thus, one of the assumptions of the method in Sec. IV is violated. This leads to the result

$$M^{\rm att}_+(v) \simeq \frac{r_-^3}{12\xi}\log\left(y_0 v^{-p}\right)^2. \tag{87}$$

The constant y_0 is the solution of the transcendental equation

$$3a + by_0 + \frac{1}{2}\kappa_- y_0 \log(y_0)^2 = 0. \tag{88}$$

Here the constants a and b encode properties of the background geometry and are defined in Eq. (C5).

It is remarkably that the AS-collapse model contains a phase where the buildup of the Misner-Sharp mass at the inner horizon is even slower than power law. This discovery constitutes the main finding of our work.

C. Numerical analysis

We continue the investigation of the Ori model by presenting explicit examples obtained by solving the coupled system of differential equations (18) and (24) numerically. The results corroborate the analytical results derived in the last subsection. Moreover, they show that the late-time attractors are indeed reached also from initial conditions placed outside of the scaling regimes governed by the quasifixed points. The typical timescale for reaching

TABLE III. Initial conditions used for generating the numerical integrations in Figs. 4 and 7. All values are imposed at $v_\mathrm{i} = 5$. The background geometries are fixed by settings in Table I. If appropriate, the value of the free integration constant c appearing in relation to mass-inflation or exponential attractors is added in the column c.

Solution	Final $M_+(v)$	$R(v_\mathrm{i})$	$m_+(v_\mathrm{i})$	c
Bardeen	Mass-inflation	0.5	1.2	0.146
	Mass-inflation	0.5	−2	2.197
Hayward	Polynomial attractor	0.58	0.8	Not applicable
	Polynomial attractor	0.58	$m^{\mathrm{att}}_{+,*}$	Not applicable
	Polynomial attractor	0.58	1.2	Not applicable
Dymnikova	Exponential attractor	0.8	2	0.102
	Terminates at v_*	0.8	0.5	Not applicable
	Exponential attractor	0.8	−0.5	1.133
Ghosh-Culetu	Mass-inflation	0.5	2	0.002
	Terminates at v_*	0.5	0.5	Not applicable
	Exponential attractor	0.5	−1	0.707
	Mass-inflation	0.5	−2	0.014
AS-collapse	Mass-inflation	0.5	2	8.99×10^{-3}
	Logarithmic attractor	0.5	0.5	Not applicable
	Logarithmic attractor	0.5	−0.5	Not applicable
	Mass-inflation	0.5	−2	0.01

the attractor is set by the surface gravity κ_- which is set to unity in all our examples. Throughout this section, we restrict the discussion to the mass $m_+(v)$ and the Misner-Sharp mass $M_+(v) \equiv M_+[R(v), m_+(v)]$. The latter is constructed by evaluating (3) on the numerical solutions for $\{R(v), m_+(v)\}$.[4] We do not plot results for the curvature scalars (A3)–(A5). Their scaling behavior readily follows from the one of $M_+(v)$. Since there are no cancellations between the single terms, this is straightforward and does not lead to additional insights.

We proceed by discussing the examples shown in Figs. 4 and 7 for different regular black-hole backgrounds. Relevant ending states in M_-+ are superimposed as gray dashed lines. The parameters specifying the regular black-hole geometries are again the ones given in Table I. The initial conditions generating the specific examples are collected in Table III.

Bardeen geometry (first line of Fig. 4*)*. The dynamics of $m_+(v)$ arising from the Bardeen geometry is displayed in the left diagram. The repulsive quasifixed point (48) has been added as the black horizontal line. The solutions are driven away from this line and their dynamics follows the asymptotics (73). The explicit value of the integration constant c is obtained by equating the numerical solution to the asymptotics at a fixed value v and list in column "c" of Table III. The absolute value of the Misner-Sharp mass evaluated at the position of the shell is shown in the right diagram. Again the asymptotic late-time behavior follows the relation (74), which is superimposed as the gray-dashed lines. This establishes that both types of solution exhibit eternal mass inflation.

Hayward geometry (second line of Fig. 4*)*. The solutions $m_+(v)$ shown in the left panel are governed by the interplay of the repulsive quasifixed point (52a) and the global attractor (52b), highlighted, respectively, as the black and gray horizontal line. Solutions for $m_+(v)$ starting above the repulsive line reach infinity at a finite value of v and subsequently reenter at minus infinity before reaching the global attractor from below. Solutions starting between the two lines approach the attractor from above. The reconstruction of $M_+(v)$ at the position of the shell is shown in the right diagram. Both solutions approaching $m^{\mathrm{att}}_{+,*}$ from above and below undergo a phase of transient mass inflation before entering the polynomial scaling regime induced by the attractive quasifixed point. One can find special solutions that start tracking the polynomial attractor early on, so that the episode of transient mass inflation is shorter. An example for this is the solution added as the dashed green line. The trajectory starts on $m^{\mathrm{att}}_{+,*}$ and leads to the curve $M_+(v)$ reaching the attractor first.

Dymnikova geometry (third line of Fig. 4*)*. Similarly to the Hayward geometry, the dynamics of $m_+(v)$ in the Dymnikova case is dictated by the interplay of the repulsive quasifixed point (55) and attractive quasifixed point (56). Solutions above the repulsive line leave the phase space at the top and reenter at the bottom before reaching the attractor from below. Solutions starting between the lines approach the attractor from above and reach $m^{\mathrm{att}}_{+,*} = 0$ at finite v_*. This new feature is highlighted by the brown line. The Misner-Sharp mass evaluated along the solutions $\{R(v), m_+(v)\}$ is shown in the right panel. The numerical examples establish that solutions reaching $m^{\mathrm{att}}_{+,*}$ from below follow the asymptotic behavior (79) with the integration constants c given in Table III. Thus, we conclude that all solutions of the Dymnikova geometry reaching $v = \infty$ exhibit eternal mass inflation due to an exponential attractor.

*Ghosh-Culetu geometry (*Fig. 7 in Appendix B*)*. The late-time behavior of trajectories $m_+(v)$ is determined by the poles distributed along the curve (65), in addition to the repulsive quasifixed point (61) and the attractive one (62). Solutions defined for initial conditions above the repulsive line or below the curve will give rise to mass-inflation instability with opposite sign, similarly to the Bardeen case. Integrations starting between the repulsive line and the attractive one meet a discontinuity at finite v_*. Solutions related to initial conditions $-\alpha^2/[R(v_i)] < m_+(v_i) < 0$ (green curve in Fig. 7) sink into the attractor. The numerical analysis of $M_+(v)$ confirms that the attractor induces the

[4]The construction of $M_+(v)$ requires solving the coupled system of differential equations with high numerical precision. This applies in particular to the AS-collapse model where one encounters cancellations among leading contributions within the argument of the logarithm.

exponential scaling (80). Ultimately, all continuous solutions exhibit eternal mass inflation.

AS-collapse geometry (fourth line of Fig. 4*)*. The three quasifixed points (68) governing the dynamics of $m_+(v)$ are again shown as gray and black horizontal lines. Solutions above and below the repulsive lines go off to infinity. In addition, there are the solutions sandwiched between the repulsive lines that asymptote to the attractor $m^{\mathrm{att}}_{+,*}$. Reconstructing $M_+(v)$, we find that the first class of solutions follows the asymptotics (86) and leads to eternal mass inflation. The second class leads to a logarithmic growth of $M_+(v)$ following (87). The constant y_0 determining the position of the attractor is obtained by solving Eq. (88) numerically, yielding $y_0 = 31.549$. The attractor does not come with a free parameter. Hence the asymptotics is universal and independent of the initial conditions as long as the solution is within this class. Remarkably, the attractor can be reached without an appreciable episode of transient mass inflation. Thus, the numerical integrations confirm that the logarithmic attractor tames the mass-inflation instability completely.

We close this section with the following observation. A remarkable outcome of our phase-space analysis is that, despite substantial differences in the geometry, there are just three different types of asymptotic scaling behavior of the Misner-Sharp mass. These are summarized in Fig. 5. They comprise eternal mass inflation where M_+ grows exponentially in v, the polynomial attractor where M_+ grows as a power law, and the logarithmic attractor.

D. Singularity strength

The asymptotic late-time behaviors determined in Sec. V B readily allow one to determine the buildup of curvature singularities in the future sector of the shell. For this purpose, we evaluate the Kretschmann scalar K, the square of the Weyl-tensor C^2, and the Coulomb component of the Weyl tensor Ψ_2 introduced in Appendix A. The last two also serve as measures for the tidal distortion experienced by an object of finite proper length.

The results obtained from evaluating the general formulas (A4), (A5), and (A7) are listed in the last three columns of Table II. These reveal the following systematics. The exponential growth of $M_+(v)$ induces an exponential growth of the curvature scalars and Ψ_2. Analogously, the power-law scaling induced by the attractive quasifixed point in the Hayward model also carries over to the curvature. The case I found in the AS collapse is special since the Weyl-tensor based curvature invariant asymptote to constant, nonzero, values. Comparing the Kretschmann scalar to the Weyl-curvature squared, one observes that the log terms responsible for the exponential growth of the Kretschmann scalar are absent in the latter case. Finally, the case II found in the AS collapse shows that the logarithmic attractor induces for the curvature a power-law scaling (milder than the one for the curvature in Hayward).

At this stage it is instructive to relate these results to the classification of singularities provided by Tipler [52] and Królak [53,54,56]. Following the analysis made in [50], one finds that one can always find a coordinate system that is regular in the future sector of the shell. As a consequence, all curvature singularities building up dynamically are weak in the Tipler sense. Physically speaking, this entails that tidal forces do not diverge at the CH.

Determining the strength of the singularity within the Królak classification requires the relation between the coordinate v and the proper time τ measured by a massive observer moving along a radial geodesic in the future sector of the shell. It thereby turns out that, at asymptotically late times, this relation is given by

$$\tau \propto e^{-\kappa_- v}, \tag{89}$$

independently of the underlying dynamics of the model. This result has two profound consequences. First, the observer can reach $v = \infty$ in finite proper time. Hence the strength of the singularity is relevant when investigating whether a geodesic can be continued beyond this point. Second, the strength of the singularity can be determined by rewriting the scaling behavior in v in terms of τ. This establishes that the singularities related to an exponential growth of the curvature scalars are strong in the Królak definition. Conversely, power-law or slower than power-law growth in v indicates a weak singularity in this classification. We illustrate this based on the attractive quasifixed point appearing in the AS-collapse model. Rewriting the square of the Weyl tensor in terms of τ yields

$$C_+^2 \propto (\log \tau)^{4p}. \tag{90}$$

Thus C_+^2 becomes regular at $\tau = 0$ when it is integrated with respect to proper time once. This signals that the singularity is Królak weak. Physically, this entails that the expansion of a congruence of geodesics does not (negatively) diverge at the CH. This is a further hint that there may be a C^1 continuation of geodesics beyond this point, since an object of finite proper length would not suffer an infinite compression by tidal forces.

VI. CONCLUSION AND OUTLOOK

In this work, we studied the approach to the CH in a set of representative regular black-hole geometries: Bardeen, Hayward, Dymnikova, the Ghosh-Culetu (Minkowski-core) model, and the collapse profile inspired by asymptotic safety. We have used Ori's thin-shell implementation of the Poisson-Israel cross-flow scenario for a perturbed geometry. Within this framework, the late-time dynamics is organized by *quasifixed points*, detected in the evolution of $R(v)$ and $m_+(v)$. These quasifixed points act as late-time repellers or attractors and thereby provide a compact, model-independent way of classifying the end-state of the flow.

It turns out that there is no systematic relation between the fate of the CH stability and the core type of the geometry. The former is controlled by fixed points determined by the *functional form* of $M(r)$. Their nature and induced scaling are bound to the *exact* evolution equation of M_+. Ultimately, the stability of the black-hole interior thus depends on a global feature of the geometry. This is not a counterintuitive result: it is enough to recall that it is a localized phenomenon—the resolution of the central singularity—that produces the presence itself of the CH, which in turn affects the causal structure of the entire spacetime [23,57].

A central outcome of our phase-space analysis is a striking universality in the possible late-time growth of the Misner-Sharp mass at the CH. Across all models considered, M_+ falls into three distinct asymptotic classes: (i) the standard mass-inflation regime with exponential growth in v, (ii) a softened regime with power-law growth induced by attractors of the type identified in Ref. [50], and (iii) a new regime with logarithmic growth, realized in the AS-collapse model.

The last case is tied to a qualitative structural difference of the AS profile, in particular to the logarithmic functional form of $M(r)$, which translates into $M_+^{\mathrm{att}}(v) \sim (r_-^3/12\xi)\log(v^{-p})^2$. Remarkably, in this model the logarithmic branch is reached without a substantial transient phase of exponential mass inflation, distinguishing it sharply from regular geometries that exhibit power-law attractors [73,74]. Thus, it holds $M_+(v) \approx m_0$ both in the brief inflationary phase and when the attractor is reached, as well as in the entire regime controlled by the attractor.

Furthermore, our study shows that the tamed scalings are reached by quite generic initial conditions, satisfying $|M_+(v_i)| \ll m_0$. These are the physically meaningful initial conditions for perturbations. The size of the green clusters, discovered only *a posteriori* via Figs. 3 and 6, shows that the taming of the CH instability, when it occurs, is not due to some fine-tuning, but rather the general dynamics of the black hole interior.

Turning to curvature diagnostics, exponential growth of $M_+(v)$ yields the familiar mass-inflation-type null singularity at the CH, whereas the power-law and logarithmic phases lead to a milder divergence of curvature invariants. In all cases where curvature invariants diverge, the spacetime cannot be extended as a solution with curvature controlled in the usual sense (e.g., a C^2 extension). At the same time, the singularities are weak in the Tipler sense, and in the softened (power-law/logarithmic) regimes also weak in the Królak sense, so that geodesic completeness is not excluded at the level of this effective description, thanks to the intensity of tidal forces being finite.

As for future prospects, a challenging step would be to remove from the study of the problem the *a priori* assumption that a (past-complete) CH exists, by studying fully dynamical collapse with simultaneous ingoing and outgoing classical fluxes, where the formation (or elimination) of an inner horizon is determined self-consistently by full backreaction. Second, it would be interesting to check if the transient mass-inflation effect, which has been found recently for quasilocal apparent inner horizons [75], adopting nonstationary specific metrics, extends to other background geometries, since we have shown, in the case of the teleological CH, that the response to a perturbation strongly depends on the specific form of the mass function. Third, it would be important to explore whether the universality classes identified here persist once quantum fields and their backreaction are incorporated.

Finally, in the speculative scenario where full stability and traversability of the CH are obtained for a regular black-hole dynamics, the problem of formulating proposals for the type of physics existing beyond the CH itself will have to be faced. We hope to come back to these issues in future investigations.

ACKNOWLEDGMENTS

A. P. thanks Francesco Di Filippo and Jesse van der Duin for useful discussions. A. P. acknowledges partial financial support by Erasmus+ Grants No. 2022-1-IT02-KA131-HED-000066529 and No. 2023-1-IT02-KA131-HED-000135582.

DATA AVAILABILITY

There are no publicly available research data or software supporting this manuscript. Requests for further information or data should be sent to the authors.

APPENDIX A: CURVATURE INVARIANTS

The geometries studied in this work are of the type

$$ds^2 = -f(v,r)dv^2 + 2drdv + r^2 d\Omega^2, \qquad \text{(A1)}$$

where

$$f(v,r) = 1 - \frac{2M(v,r)}{r}. \qquad \text{(A2)}$$

In order to quantify the curvature of spacetime, we introduce the Riemann tensor $R_{\alpha\beta\gamma\delta}$, the Ricci tensor $R_{\mu\nu} = R^{\alpha}{}_{\mu\alpha\nu}$ and the Ricci scalar $R \equiv g^{\mu\nu}R_{\mu\nu}$. Furthermore, we use a prime to denote derivatives with respect to r, i.e. $M'(v,r) \equiv \partial M(v,r)/\partial r$.

For the geometry (A2) the Ricci scalar can be given in terms of the Misner-Sharp mass as

$$R = \frac{2rM'' + 4M'}{r^2}. \tag{A3}$$

In addition, we introduce the two curvature scalars at quadratic order in the spacetime curvature. The Kretschmann scalar $K \equiv R_{\alpha\beta\gamma\delta}R^{\alpha\beta\gamma\delta}$ evaluates to

$$K = \frac{48M^2}{r^6} - \frac{64MM'}{r^5} + \frac{32(M')^2}{r^4} + \frac{16MM''}{r^4} - \frac{16M'M''}{r^3} + \frac{4(M'')^2}{r^2}, \tag{A4}$$

and the square of the Weyl-tensor $C^2 \equiv C_{\alpha\beta\gamma\delta}C^{\alpha\beta\gamma\delta}$ reads

$$C^2 = \frac{4(r^2M'' - 4rM' + 6M)^2}{3r^6}. \tag{A5}$$

These two quantities are related by the identity

$$K = C^2 - 2R_{\mu\nu}R^{\mu\nu} + \frac{1}{3}R^2. \tag{A6}$$

Since the Reissner-Nordström solution and the regular black hole solutions are not Ricci flat ($R_{\mu\nu} \neq 0$), they describe two different aspects of spacetime and in principle could exhibit different behaviors as consequence of the perturbation. Finally, we also introduce the Coulomb-component Ψ_2. In the coordinate systems used in this work $\Psi_2 = -\frac{1}{2}C^{\theta\varphi}{}_{\theta\varphi}$. Written in terms of the Misner-Sharp mass one then has

$$\Psi_2 = -\frac{M}{r^3} + \frac{2M'}{3r^2} - \frac{M''}{6r}. \tag{A7}$$

Both C^2 and Ψ_2 give measures for the tidal forces experienced by a massive object.

APPENDIX B: FIGURES FOR THE GHOSH-CULETU GEOMETRY

The Ghosh-Culetu geometry stands as a test case for a qualitatively different regularization mechanism of the central singularity. It features a Minkowski core [33–35,57]. The phase space of the Ghosh-Culetu geometry is depicted in Fig. 6, while examples of solutions for $m_+(v)$ and $M_+(v)$ are displayed in Fig. 7. Our analysis shows that the relevant feature for the stability properties of the CH is the full functional form of $M(r)$, which induces a certain nonlinearity in the rhs of (24), and not its small-r expansion. The phases identified for this model are tabulated in Table II.

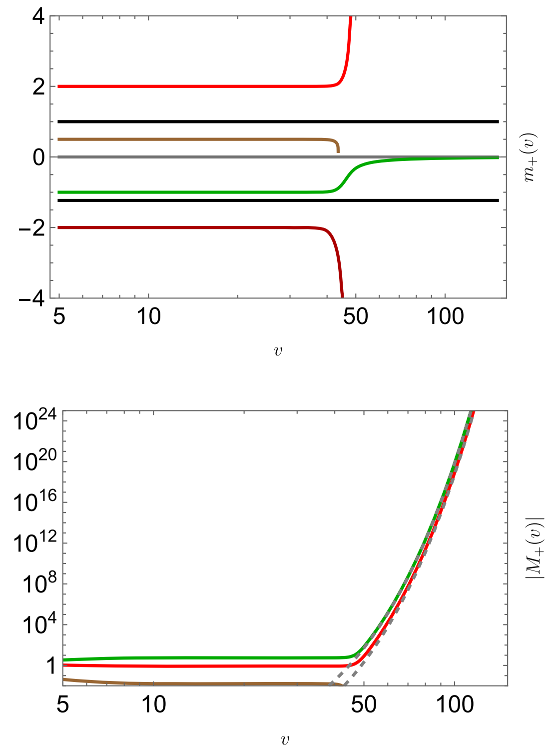

FIG. 7. Illustrations of $m_+(v)$ (top panel) and the absolute value of $M_+(v)$ (bottom panel) on a double-logarithmic scale. The initial conditions for the numerical integrations are set as indicated in Table III. In the top panel, the repulsive black line of negative value $m_+(v_i) = -1.23$ is taken as sample from the curve $m_+(v_i) = -\alpha^2/R(v_i)$, for $R(v_i) = 0.5$.

APPENDIX C: ATTRACTOR FOR THE AS-COLLAPSE

This appendix provides the details underlying the derivation that the late-time attractor (68c) induces the logarithmic divergence of the Misner-Sharp mass given in (87).

We start from Eq. (66) which encodes the dynamics of $m_+(v)$. The late-time attractor (68b) is characterized by

$$\left(1 + \frac{6\xi m_+}{R^3}\right) \ll 1. \tag{C1}$$

This motivates introducing the new function

$$x(v) \equiv 1 + \frac{6\xi m_+(v)}{R(v)^3}. \tag{C2}$$

Recasting Eq. (66) in terms of this new function yields

$$\dot{x} = 3(1-x)\frac{\dot{R}}{R} + \frac{6\xi}{R^3}x\left(1 - \frac{R^2}{6\xi}\log x^2\right)F(v). \tag{C3}$$

At this stage, no approximation has been made. Subsequently, we approximate R, $\dot{R}$, and $F(v)$ by their leading late-time behavior

$$R \simeq r_-, \qquad \dot{R} \simeq (1-p)\frac{a_0}{v^p}, \qquad F(v) \simeq -\frac{r_- \kappa_-}{2}, \tag{C4}$$

with a_0 given in Eq. (33a). Introducing the abbreviations

$$a = -\frac{(p-1)\beta}{\kappa_- r_-^3}\left(1+\frac{6m_0\xi}{r_-^3}\right)^{-1}, \qquad b \equiv -\frac{3\xi\kappa_-}{r_-^2}, \tag{C5}$$

the equation encoding the late-time dynamics of $x(v)$ reads

$$\dot{x} = 3av^{-p} + bx + \frac{\kappa_-}{2}x\log(x^2). \tag{C6}$$

Here the term proportional to $x\dot{R}$ has been dropped since it does not contribute to the leading behavior at late times. Unfortunately, we are not aware of an analytic solution of (C6).

In order to progress further, we decompose

$$x(v) = \frac{1}{v^t}y(v), \tag{C7}$$

where t is a free coefficient capturing the power-law scaling of $x(v)$. We then recast (C6) in terms of the scaling operator associated with $y(v)$,

$$\begin{aligned}\frac{d\log y}{d\log v} = t + 3ay^{-1}v^{t+1-p} + bv \\ + \frac{\kappa_-}{2}v\log y^2 - t\kappa_- v\log v.\end{aligned} \tag{C8}$$

At this point, let us assume that $y(v) = y_0$ is a v-independent constant. This is equivalent to the assumption that $x(v)$ exhibits a power-law behavior at late times. Under this assumption, the left-hand side of (C8) vanishes. Requiring that the terms containing just powers of v on the rhs cancel then fixes

$$t = p, \tag{C9}$$

and

$$a + by_0 + \frac{1}{2}\kappa_- y_0\log(y_0)^2 = 0. \tag{C10}$$

The assumption $y(v) = y_0$ cannot be entirely correct, though, since it does not account for the $v\log v$ term appearing in the last line of Eq. (C8). These contributions can be consistently accounted for by generalizing our initial assumption to

$$y(v) = y_0\left[1 + \sum_{n=1} y_n \log^n(v)\right], \tag{C11}$$

where y_n are free coefficients. The new terms in (C11) then induce logarithmic corrections to the power-law scaling of $x(v)$. Substituting (C11) into (C8) we arrive at

$$\begin{aligned}\frac{d\log\tilde{y}}{d\log v} = 12 + \frac{3a}{y_0}v\left(\frac{1}{\tilde{y}}-1\right) \\ + \kappa_- v\log\tilde{y} - 12\kappa_- v\log v.\end{aligned} \tag{C12}$$

Here, we abbreviated $\tilde{y} \equiv [1 + \sum_{n=1} y_n \log^n(v)]$ and used (C10) to eliminate the terms linear in v. Notably, the left-hand side and the first term on the rhs of (C12) are subleading in the late-time dynamics and can be dropped. The remainder of the equation reads

$$\frac{3a}{y_0}v\left(\frac{1}{\tilde{y}}-1\right) + \kappa_- v\log\tilde{y} - 12\kappa_- v\log v = 0. \tag{C13}$$

This equation has the status of a generating functional that fixes the free coefficients y_n. Expanding in powers of $\log v$, one obtains a hierarchy of equation that allows to fix all y_n recursively, by solving linear equations. The $v\log v$ term thereby serves as a seed that excludes the trivial solution. The structure of (C13) also shows that the generalization (C11) is sufficient to capture the late-time dynamics of the attractor.

When reconstructing the Misner-Sharp mass $M_+(v)$, one then takes into account that inserting the product (C11) into the logarithm turns the bracket into an additive (and subleading) contribution. In this way, one establishes that (87) provides a well-founded approximation of the late-time dynamics associated with the attractive quasifixed point of the model.

[1] S. W. Hawking and G. F. R. Ellis, *The Large Scale Structure of Space-Time*, Cambridge Monographs on Mathematical Physics (Cambridge University Press, Cambridge, England, 2023).

[2] N. Afshordi *et al.*, Black holes inside and out 2024: Visions for the future of black hole physics, arXiv:2410.14414.

[3] R. Penrose, Structure of space-time, in *Battelle Rencontres—1967 Lectures in Mathematics and Physics: Seattle, WA, USA* (Benjamin, New York, 1968), pp. 121–235.

[4] E. Poisson and W. Israel, Inner-horizon instability and mass inflation in black holes, Phys. Rev. Lett. **63**, 1663 (1989).

[5] E. Poisson and W. Israel, Internal structure of black holes, Phys. Rev. D **41**, 1796 (1990).

[6] A. Ori, Inner structure of a charged black hole: An exact mass-inflation solution, Phys. Rev. Lett. **67**, 789 (1991).

[7] R. Balbinot and E. Poisson, Mass inflation: The semiclassical regime, Phys. Rev. Lett. **70**, 13 (1993).

[8] M. Casals, A. Fabbri, C. Martínez, and J. Zanelli, Quantum backreaction on three-dimensional black holes and naked singularities, Phys. Rev. Lett. **118**, 131102 (2017).

[9] M. Casals, A. Fabbri, C. Martínez, and J. Zanelli, Quantum fields as cosmic censors in $(2+1)$-dimensions, Int. J. Mod. Phys. D **27**, 1843011 (2018).

[10] O. Sela, Quantum effects near the Cauchy horizon of a Reissner-Nordström black hole, Phys. Rev. D **98**, 024025 (2018).

[11] M. Casals, A. Fabbri, C. Martínez, and J. Zanelli, Quantum-corrected rotating black holes and naked singularities in $(2+1)$ dimensions, Phys. Rev. D **99**, 104023 (2019).

[12] N. Zilberman, A. Levi, and A. Ori, Quantum fluxes at the inner horizon of a spherical charged black hole, Phys. Rev. Lett. **124**, 171302 (2020).

[13] C. Klein, J. Zahn, and S. Hollands, Quantum (dis)charge of black hole interiors, Phys. Rev. Lett. **127**, 231301 (2021).

[14] C. Barceló, V. Boyanov, R. Carballo-Rubio, and L. J. Garay, Classical mass inflation versus semiclassical inner horizon inflation, Phys. Rev. D **106**, 124006 (2022).

[15] N. Zilberman, M. Casals, A. Ori, and A. C. Ottewill, Quantum fluxes at the inner horizon of a spinning black hole, Phys. Rev. Lett. **129**, 261102 (2022).

[16] C. Klein, M. Soltani, M. Casals, and S. Hollands, Infinite quantum twisting at the Cauchy horizon of rotating black holes, Phys. Rev. Lett. **132**, 121501 (2024).

[17] J. Arrechea, G. Neri, and S. Liberati, Inner horizon instability via the trace anomaly effective action, Phys. Rev. D **111**, 084036 (2025).

[18] S. Hollands, R. M. Wald, and J. Zahn, Quantum instability of the Cauchy horizon in Reissner–Nordström–deSitter spacetime, Classical Quantum Gravity **37**, 115009 (2020).

[19] S. Hollands, C. Klein, and J. Zahn, Quantum stress tensor at the Cauchy horizon of the Reissner–Nordström–de Sitter spacetime, Phys. Rev. D **102**, 085004 (2020).

[20] J. Bardeen, Non-singular general relativistic gravitational collapse, in *Proceedings of the 5th International Conference on Gravitation and the Theory of Relativity* (Tbilisi University Press, Georgian SSR (Soviet Socialist Republic), USSR, 1968), p. 87.

[21] E. Ayon-Beato and A. Garcia, The Bardeen model as a nonlinear magnetic monopole, Phys. Lett. B **493**, 149 (2000).

[22] S. Ansoldi, Spherical black holes with regular center: A Review of existing models including a recent realization with Gaussian sources, in *Conference on Black Holes and Naked Singularities* (2008), arXiv:0802.0330.

[23] R. Carballo-Rubio, F. Di Filippo, S. Liberati, and M. Visser, Geodesically complete black holes, Phys. Rev. D **101**, 084047 (2020).

[24] *Regular Black Holes. Towards a New Paradigm of Gravitational Collapse*, edited by C. Bambi, Springer Series in Astrophysics and Cosmology (Springer, New York, 2023).

[25] C. Lan, H. Yang, Y. Guo, and Y.-G. Miao, Regular black holes: A short topic review, Int. J. Theor. Phys. **62**, 202 (2023).

[26] R. Carballo-Rubio *et al.*, Towards a non-singular paradigm of black hole physics, arXiv:2501.05505.

[27] I. Dymnikova, Vacuum nonsingular black hole, Gen. Relativ. Gravit. **24**, 235 (1992).

[28] I. Dymnikova, Cosmological term as a source of mass, Classical Quantum Gravity **19**, 725 (2002).

[29] A. Platania, Dynamical renormalization of black-hole spacetimes, Eur. Phys. J. C **79**, 470 (2019).

[30] A. Bonanno and M. Reuter, Renormalization group improved black hole space-times, Phys. Rev. D **62**, 043008 (2000).

[31] B. Koch and F. Saueressig, Black holes within asymptotic safety, Int. J. Mod. Phys. A **29**, 1430011 (2014).

[32] S. A. Hayward, Formation and evaporation of regular black holes, Phys. Rev. Lett. **96**, 031103 (2006).

[33] A. Simpson and M. Visser, Regular black holes with asymptotically Minkowski cores, Universe **6**, 8 (2019).

[34] H. Culetu, On a regular charged black hole with a nonlinear electric source, Int. J. Theor. Phys. **54**, 2855 (2015).

[35] S. G. Ghosh, A nonsingular rotating black hole, Eur. Phys. J. C **75**, 532 (2015).

[36] D. V. Singh, S. G. Ghosh, and S. D. Maharaj, Exact nonsingular black holes and thermodynamics, Nucl. Phys. **B981**, 115854 (2022).

[37] A. Bonanno, D. Malafarina, and A. Panassiti, Dust collapse in asymptotic safety: A path to regular black holes, Phys. Rev. Lett. **132**, 031401 (2024).

[38] E. Ayon-Beato and A. Garcia, Regular black hole in general relativity coupled to nonlinear electrodynamics, Phys. Rev. Lett. **80**, 5056 (1998).

[39] I. Dymnikova, Regular electrically charged structures in nonlinear electrodynamics coupled to general relativity, Classical Quantum Gravity **21**, 4417 (2004).

[40] K. A. Bronnikov, Regular black holes sourced by nonlinear electrodynamics, arXiv:2211.00743.

[41] D. Malafarina and B. Toshmatov, Connection between regular black holes in nonlinear electrodynamics and semiclassical dust collapse, Phys. Rev. D **105**, L121502 (2022).

[42] P. Bueno, P. A. Cano, and R. A. Hennigar, Regular black holes from pure gravity, Phys. Lett. B **861**, 139260 (2025).

[43] R. Casadio, A. Giusti, and J. Ovalle, Quantum Reissner-Nordström geometry: Singularity and Cauchy horizon, Phys. Rev. D **105**, 124026 (2022).

[44] M. Calzá, M. Rinaldi, and S. Zerbini, Topological regular black holes without a Cauchy horizon, Phys. Rev. D **112**, 024024 (2025).
[45] R. Carballo-Rubio, F. Di Filippo, S. Liberati, C. Pacilio, and M. Visser, On the viability of regular black holes, J. High Energy Phys. 07 (2018) 023.
[46] R. Carballo-Rubio, F. Di Filippo, S. Liberati, C. Pacilio, and M. Visser, Inner horizon instability and the unstable cores of regular black holes, J. High Energy Phys. 05 (2021) 132.
[47] F. Di Filippo, R. Carballo-Rubio, S. Liberati, C. Pacilio, and M. Visser, On the inner horizon instability of non-singular black holes, Universe **8**, 204 (2022).
[48] A. J. S. Hamilton and P. P. Avelino, The physics of the relativistic counter-streaming instability that drives mass inflation inside black holes, Phys. Rep. **495**, 1 (2010).
[49] A. Bonanno and F. Saueressig, Stability properties of regular black holes, arXiv:2211.09192.
[50] A. Bonanno, A.-P. Khosravi, and F. Saueressig, Regular black holes with stable cores, Phys. Rev. D **103**, 124027 (2021).
[51] A. Bonanno, A.-P. Khosravi, and F. Saueressig, Regular evaporating black holes with stable cores, Phys. Rev. D **107**, 024005 (2023).
[52] F. J. Tipler, Singularities in conformally flat spacetimes, Phys. Lett. **64A**, 8 (1977).
[53] A. Krolak, Towards the proof of the cosmic censorship hypothesis, Classical Quantum Gravity **3**, 267 (1986).
[54] A. Krolak, Towards the proof of the cosmic censorship hypothesis in cosmological space-times, J. Math. Phys. (N.Y.) **28**, 138 (1987).
[55] A. Bonanno, S. Droz, W. Israel, and S. M. Morsink, Structure of the spherical black hole interior, Proc. R. Soc. A **450**, 553 (1995).
[56] L. M. Burko, Strength of the null singularity inside black holes, Phys. Rev. D **60**, 104033 (1999).
[57] A. Panassiti, Regular black hole cores via gravitational evanescence of collapsing matter, Phys. Rev. D **113**, 064057 (2026).
[58] M. A. Markov, Limiting density of matter as a universal law of nature, Pis'ma Zh. Eksp. Teor. Fiz. **36**, 214 (1982).
[59] M. A. Markov, Problems of a perpetually oscillating universe, Ann. Phys. (N.Y.) **155**, 333 (1984).
[60] V. P. Frolov, M. A. Markov, and V. F. Mukhanov, Through a black hole into a new universe?, Phys. Lett. B **216**, 272 (1989).
[61] V. P. Frolov, M. A. Markov, and V. F. Mukhanov, Black holes as possible sources of closed and semiclosed worlds, Phys. Rev. D **41**, 383 (1990).
[62] V. P. Frolov, Notes on nonsingular models of black holes, Phys. Rev. D **94**, 104056 (2016).
[63] P. Bueno, P. A. Cano, R. A. Hennigar, and Á. J. Murcia, Dynamical formation of regular black holes, Phys. Rev. Lett. **134**, 181401 (2025).
[64] R. Percacci, *An Introduction to Covariant Quantum Gravity and Asymptotic Safety*, 100 Years of General Relativity Vol. 3 (World Scientific, Singapore, 2017).
[65] M. Reuter and F. Saueressig, *Quantum Gravity and the Functional Renormalization Group: The Road towards Asymptotic Safety* (Cambridge University Press, Cambridge, England, 2019).
[66] C. Wetterich, Quantum scale symmetry, arXiv:1901.04741.
[67] A. Eichhorn and M. Schiffer, Asymptotic safety of gravity with matter, arXiv:2212.07456.
[68] A. Bonanno, T. Denz, J. M. Pawlowski, and M. Reichert, Reconstructing the graviton, SciPost Phys. **12**, 001 (2022).
[69] A. Bonanno, A. Eichhorn, H. Gies, J. M. Pawlowski, R. Percacci, M. Reuter, F. Saueressig, and G. P. Vacca, Critical reflections on asymptotically safe gravity, Front. Phys. **8**, 269 (2020).
[70] C. Barrabes and W. Israel, Thin shells in general relativity and cosmology: The lightlike limit, Phys. Rev. D **43**, 1129 (1991).
[71] R. H. Price, Nonspherical perturbations of relativistic gravitational collapse. 1. Scalar and gravitational perturbations, Phys. Rev. D **5**, 2419 (1972).
[72] R. H. Price, Nonspherical perturbations of relativistic gravitational collapse. II. Integer-spin, zero-rest-mass fields, Phys. Rev. D **5**, 2439 (1972).
[73] A. Bonanno, A.-P. Khosravi, and F. Saueressig, Reply to "Comment on 'Regular evaporating black holes with stable cores'", Phys. Rev. D **108**, 128502 (2023).
[74] R. Carballo-Rubio, F. Di Filippo, S. Liberati, C. Pacilio, and M. Visser, Comment on "Regular evaporating black holes with stable cores", Phys. Rev. D **108**, 128501 (2023).
[75] R. Carballo-Rubio, F. Di Filippo, S. Liberati, and M. Visser, Mass inflation without Cauchy horizons, Phys. Rev. Lett. **133**, 181402 (2024).